

Article

Application of Electromagnetic Methods for Reservoir Monitoring with Emphasis on Carbon Capture, Utilization, and Storage

César Barajas-Olalde ^{1,*}, Donald C. Adams ¹, Ana Curcio ², Sofia Davydycheva ³, Ryan J. Klapperich ¹, Yardenia Martinez ³, Andri Y. Paembonan ^{3,4}, Wesley D. Peck ¹, Kurt Strack ^{3,*} and Pantelis Soupios ⁵

¹ Energy & Environmental Research Center, 15 North 23rd Street, Stop 9018, Grand Forks, ND 58202, USA; dadams@undeerc.org (D.C.A.); wpeck@undeerc.org (W.D.P.)

² Proingeo SA, Agüero 1995 6A, Ciudad Autónoma de Buenos Aires 1425, Argentina; anitacurcio@gmail.com

³ KMS Technologies, Inc., 11999 Katy Freeway, Suite 160, Houston, TX 77079, USA; sdavyd@gmail.com (S.D.); yardenia@kmstechnologies.com (Y.M.); andriyadip@gmail.com (A.Y.P.)

⁴ Sumatera Institute of Technology, Selatan 35365, Indonesia

⁵ Department of Geosciences, College of Petroleum Engineering and Geosciences, King Fahd University of Petroleum and Minerals, Dhahran 31261, Saudi Arabia; p.soupios@gmail.com

* Correspondence: cbarajas@undeerc.org (C.B.-O.); kurt@kmstechnologies.com (K.S.); Tel.: +1-701-777-5414 (C.B.-O.); +1-832-630-8144 (K.S.)

Abstract: The Controlled-Source ElectroMagnetic (CSEM) method provides crucial information about reservoir fluids and their spatial distribution. Carbon dioxide (CO₂) storage, enhanced oil recovery (EOR), geothermal exploration, and lithium exploration are ideal applications for the CSEM method. The versatility of CSEM permits its customization to specific reservoir objectives by selecting the appropriate components of a multi-component system. To effectively tailor the CSEM approach, it is essential to determine whether the primary target reservoir is resistive or conductive. This task is relatively straightforward in CO₂ monitoring, where the injected fluid is resistive. However, for scenarios involving brine-saturated (water-wet) or oil-wet (carbon capture, utilization, and storage—CCUS) reservoirs, consideration must also be given to conductive reservoir components. The optimization of data acquisition before the survey involves analyzing target parameters and the sensitivity of multi-component CSEM. This optimization process typically includes on-site noise measurements and 3D anisotropic modeling. Based on our experience, subsequent surveys tend to proceed smoothly, yielding robust measurements that align with scientific objectives. Other critical aspects to be considered are using magnetotelluric (MT) measurements to define the overall background resistivities and integrating real-time quality assurance during data acquisition with 3D modeling. This integration allows the fine tuning of acquisition parameters such as acquisition time and necessary repeats. As a result, data can be examined in real-time to assess subsurface information content while the acquisition is ongoing. Consequently, high-quality data sets are usually obtained for subsequent processing and initial interpretation with minimal user intervention. The implementation of sensitivity analysis during the inversion process plays a pivotal role in ensuring that the acquired data accurately respond to the target reservoirs' expected depth range. To elucidate these concepts, we present an illustrative example from a CO₂ storage site in North Dakota, USA, wherein the long-offset transient electromagnetic method (LOTEM), a variation of the CSEM method, and the MT method were utilized. This example showcases how surface measurements attain appropriately upscaled log-scale sensitivity. Furthermore, the sensitivity of the CSEM and MT methods was examined in other case histories, where the target reservoirs exhibited conductive properties, such as those encountered in enhanced oil recovery (EOR), geothermal, and lithium exploration applications. The same equipment specifications were utilized for CSEM and MT surveys across all case studies.



Citation: Barajas-Olalde, C.; Adams, D.C.; Curcio, A.; Davydycheva, S.; Klapperich, R.J.; Martinez, Y.; Paembonan, A.Y.; Peck, W.D.; Strack, K.; Soupios, P. Application of Electromagnetic Methods for Reservoir Monitoring with Emphasis on Carbon Capture, Utilization, and Storage. *Minerals* **2023**, *13*, 1308. <https://doi.org/10.3390/min13101308>

Academic Editor: Paulo T. L. Menezes

Received: 4 August 2023

Revised: 27 September 2023

Accepted: 28 September 2023

Published: 10 October 2023



Copyright: © 2023 by the authors. Licensee MDPI, Basel, Switzerland. This article is an open access article distributed under the terms and conditions of the Creative Commons Attribution (CC BY) license (<https://creativecommons.org/licenses/by/4.0/>).

Keywords: CO₂ storage monitoring; fluid imaging; controlled-source electromagnetics (CSEM); magnetotelluric (MT) survey; CCUS; EOR; geothermal monitoring; lithium exploration

1. Introduction

Clean energy technology deployment must accelerate rapidly to meet climate goals [1]. Carbon capture, utilization, and storage (CCUS) technology for capturing CO₂ emissions to use them sustainably or store them is crucial for reaching net zero emissions [2]. As part of the CCUS green gas reduction strategies, injecting CO₂ into saline aquifers for storage and oil reservoirs to enhance oil recovery (CO₂-EOR) addresses the challenge of reducing atmospheric concentrations of CO₂ and satisfying the worldwide energy demand [3]. This technology permits us to store CO₂ within deep geological formations permanently. These formations must be deeper than 800 m deep, have a thick and extensive seal, sufficient porosity for large volumes, and be permeable enough to allow high flow rates without requiring excessive pressure [4]. It is worth noting that at depths of around 800 m and below, the natural temperature and fluid pressure are higher than the critical point of CO₂ (temperature 31.1 °C and pressure 72.9 atm) in most parts of the world. Supercritical CO₂ is dense like a liquid but viscous like a gas. Therefore, injecting supercritical CO₂ at this depth or lower makes storage more space-efficient [5].

Transitioning from coal and oil to geothermal energy is another priority envisioned in the Net Zero Emissions (NZE) scenario, as heat flux from the Earth's core provides a reliable and abundant green source of energy for decarbonization of the energy system [1,6]. In recent years, research efforts have been focused on assessing the advantages and efficiency of using CO₂, an alternative to water, as heat transmission fluid for geothermal energy recovery from enhanced geothermal systems (EGS) where the permeability of the underground source is enhanced by hydrofracturing. In a CO₂-EGS scenario, CO₂ geologic storage is an ancillary objective of geothermal operations ([7] and the literature herein). There are several challenges associated with transitioning to geothermal energy. One of the significant historic challenges is its dependence on specific geographical locations. Geothermal fluids cannot be transported far from their source, which limits investment in this field by developed countries. Drilling activities and the disposal of geothermal fluid can have environmental impacts, such as emitting greenhouse gases and inducing seismic activity. However, these challenges are being addressed by bringing lower enthalpy geothermal reservoirs online, developing more efficient power generation and storage technology, using efficient heat pumps, and improving geophysical technology to measure near urban areas.

CO₂-Plume Geothermal (CPG) [8,9] is another emerging technology to harvest geothermal energy by circulating CO₂ through geothermal reservoirs with naturally sufficiently porous and permeable formations overlain by caprock. In CPG systems, the key objective is to provide simultaneous CO₂-injection-induced pressure relief by producing hot brine with consumptive beneficial uses [7,10]. The CO₂-sequestration potential of CPG systems is more significant than that of CO₂-EGS systems as they utilize natural large high-permeability reservoirs such as the Williston Basin, USA [8].

The deployment of these clean energies has generated a higher demand for critical minerals [1,6]. Defining critical minerals depends on the context [11]. While lithium, nickel, cobalt, manganese, and graphite are required for developing efficient lithium-ion batteries, rare earth elements are needed for wind turbines and electric vehicles, and copper and aluminum for solar photovoltaic technology and electricity networks [2].

Geophysical methods are essential for monitoring reservoirs for CO₂ sequestration, geothermal, and EOR activities, as well as for exploring critical minerals. These methods are vital for ensuring the permanent containment of CO₂ within reservoirs and increasing the success of finding critical mineral resources. Time-lapse reflection seismics is the standard geophysical method used to monitor CO₂ plume migration due to its high horizontal resolution [12].

When CO₂ is injected into a geologic formation, the existing fluid (brine or oil) is replaced, creating an electrical resistivity contrast. Forward modeling is needed to understand whether the injected CO₂ in a brine reservoir will increase or decrease the resistivity. Figure 1 shows some models for the fluids in a CO₂ reservoir (top) [13] and the structure in

a hydrocarbon reservoir (bottom) [14]. In the CO₂ injection case, the CO₂ combines with the water in the brine and builds larger molecules [13] that are neutrally charged (colored purple in the figure). As a result, fewer electrons are available to provide current flow, and the reservoir is more resistive. In the figure on the bottom, a rock model made up of grains and pore space [14] is considered. The pores are filled with fluid, and when strain/stress are impressed upon it, the brine fluid's mobility and electron flow increase, causing a resistivity reduction. Once the pressure on the grain-to-grain contact increases, the reservoir seal breaks, generating a microseismic signal. Similar to the fluid model described above, any water saturation in the reservoir fluid contains free electrons. When the plume front moves through the reservoir, it exerts pressure on existing fluid (and even causes microseismic signals when the seal breaks). This pressure will cause the free electrons to flow and strong resistivity reduction right at the plume front, followed by the resistive plume. In the case of CCUS, this is caused by a fluid pressure wave due to the injection. Thus, CO₂ injection causes a resistive plume in a brine reservoir, and resistivity reduction at the edges can be observed.

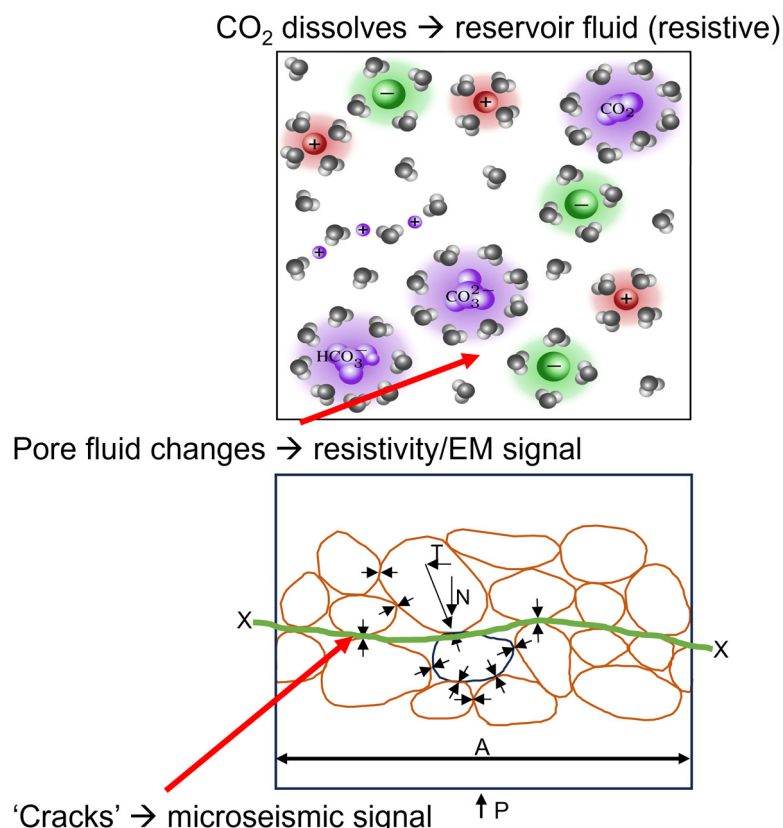


Figure 1. Rock models illustrate the pore fluid response to CO₂ injection and flooding (modified after [13,14]). The rock models focus on the fluids (top) and depict brine molecules (pore water: grey; cations: red; and anions: green) and CO₂-saturated ones (purple). Below, a model of a clastic rock with grains and pore space is displayed. The grain-to-grain contacts (green line) build the fluid boundary.

Electromagnetic (EM) methods are sensitive to resistive contrasts [15]; therefore, they are ideal for estimating the location and extent of an injected CO₂ plume. Multiple time-lapse surveys can be used to observe the change in resistivity because of the injection of CO₂ and its subsequent movement. Measurements taken before CO₂ injection can provide a baseline against which future changes can be evaluated. Time-lapse Controlled-Source ElectroMagnetic (CSEM) surveys combined with magnetotelluric (MT) surveys are a valuable tool for monitoring injected industrial CO₂ as a part of CCUS processes. Even if the changes caused by the CO₂ are small, it should be confirmed with confidence that changes

seen in the data are only because of the movement of the CO₂ and not noise sources such as naturally occurring electric fields, surveying mistakes, or local anthropogenic features.

When surface CSEM measurements are tied to 3D anisotropic models derived from the available logs and lithology from the area under investigation as part of an initial 3D feasibility workflow, baseline measurements can be verified within the context of the borehole information, representing a significant risk reduction.

An initial 3D feasibility modeling workflow includes field noise measurements to determine the noise level and, thus, the best experimental source-sensor geometry and acquisition parameters based on the expected fluid substitution models. Careful instrument calibration and verification of all acquisition parameters are essential for data acquisition. Concurrent with the acquisition, near-real-time quality assurance and control (QA/QC) are carried out. The feedback verification loop results positively influence the acquisition's data quality by optimizing operation times/equipment moves.

This process defines the proper length of acquisition time and consequently yields good data quality that can then be used for unsupervised inversion. The only influencing components in the inversion are the data weights derived from the repeated measurements (stacking weights). CSEM and MT data acquisition can benefit from this process and achieve high sensitivities for deep reservoir targets.

Achieving log scale resolution from surface measurements is a significant breakthrough; thus, baseline measurements can be verified before acquiring the monitoring measurements. Based on the results, the time-lapse (monitoring) survey can be further fine-tuned to reduce the success risk by taking the data integration from a subjective interpretation to an automated mere data display. This step requires hardware control and operation parameters (frequently repeated calibration) to obtain higher accuracy than is normal for exploration purposes.

Applying EM data acquisition systems to rare minerals exploration has demonstrated the need for careful hardware design to achieve high amplifier fidelity. This results in the ability to record subsurface responses requiring a high dynamic range from high resistivity contrast. Lithium prospecting represents such a challenge as lithium has a resistivity comparable to seawater at several hundred meters' depth. Electric and EM methods are suited for lithium prospecting due to their sensitivity to very low electrical resistivity (typically 0.1 to 0.5 ohm-m) associated with the brine-saturated multilayers present and with a frequency/time window. These methods require specific equipment characteristics (as used for time domain CSEM) with instantaneous dynamic range.

In the next sections, we present CCUS, geothermal, EOR, and critical mineral case histories using EM methods.

2. Case Histories

The initial case study exemplifies the application of a feasibility workflow to a baseline data set obtained through the long-offset transient electromagnetic method (LOTEM) [16]. This method is a variation of the CSEM method, which was integrated with the MT method for a time-lapse survey in Center, North Dakota, USA, as a part of a CCUS project. This example describes rigorous quality control and assessment methods, including noise removal and data validation with 1D and 3D inversion to tie results to borehole logs. The results are an accurate and representative CSEM data set and information that stakeholders can use to inform future time-lapse survey costs and designs.

The second case history is a geothermal example from Saudi Arabia focusing on exploration. The EOR case history examples include a modeling and feasibility study and a field test from the Middle East.

Finally, lithium exploration's critical minerals case histories in Argentina and Saudi Arabia are described. The first is from an area where lithium reserves are known, and the second is from an area where they are suspected based on our findings.

All case studies were conducted utilizing the same equipment for CSEM and MT surveys. The equipment was designed for monitoring purposes, ensuring high repeatability,

long-term stability, and minimum influence of system bandwidth limitations on signal bandwidth. The transmitter used was either a 100 (EOR example) or 150 (CCUS and Saudi Arabia examples) kVA transmitter, as described in [17]. The array acquisition system for the CSEM (LOTEM) and MT configurations is described in [18]. For more information on the system architecture and survey design, see [15]. Furthermore, additional references for data processing, data interpretation, and inversion activities considered in the case studies can be found in Appendix A.

2.1. Monitoring of CO₂ in a Saline Reservoir in North Dakota, USA

Measurements taken before CO₂ injection can provide a baseline against which future changes can be evaluated. Multiple time-lapse surveys can be used to observe the change in resistivity because of the injection of CO₂ and subsequent movement.

Baseline EM methods were applied to assess their performance in CO₂ monitoring in the lower Permian Broom Creek and Cambrian and lower Ordovician Deadwood formations in the Williston Basin near Center, North Dakota, USA. Approximately 4 million metric tons of CO₂ annually are expected to be injected into the Broom Creek and Deadwood formations at depths of approximately 1450 and 2835 m and average thicknesses of 70 m and 85 m, respectively. Figure 2 shows a simplified cross-section of North Dakota with the studied reservoirs (yellow ellipses) and a simplified stratigraphic column, including the formations overlying and underlying the studied reservoirs. The vertical black line represents the approximated location of the studied area.

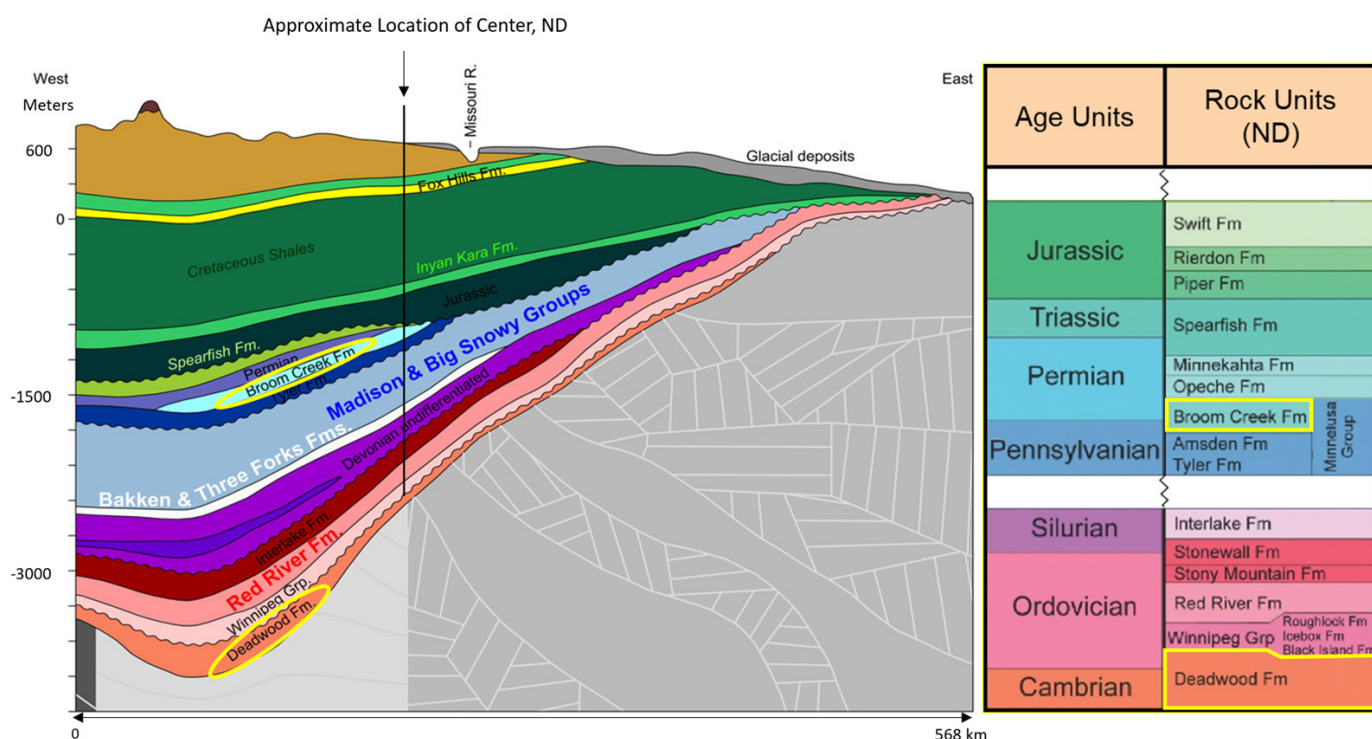


Figure 2. Simplified geologic cross-section (W–E) through the Williston basin, North Dakota (left), and simplified stratigraphic column (right). Potential CO₂ injection reservoirs are lower Permian Broom Creek and Cambrian to lower Ordovician Deadwood. (Modified after North Dakota Geological Survey—ndstudies.gov). The yellow outlines highlight the potential carbon capture and sequestration formations.

The major Broom Creek lithofacies are eolian sandstone, nearshore marine sandstone, marine carbonate, and anhydrite. The Broom Creek Formation in the study area can be divided into upper, middle, and lower sandstone-dominated intervals, with an average porosity of 23% and median permeability of 100 mD. Mudstones, siltstones, and interbed-

ded evaporites of the undifferentiated middle Permian Opeche and upper Permian–Triassic Spearfish formations unconformably overlie the Broom Creek Formation. Mudstones and siltstones of the lower Jurassic lower Piper Formation (Picard Member and lower) overlie the Opeche–Spearfish formations. The lower Piper and Opeche–Spearfish formations serve as the primary confining zone for the CO₂ storage reservoir, with an average thickness of 47 m. The upper Pennsylvanian Amsden Formation (dolostone, limestone, and anhydrite) unconformably underlies the Broom Creek Formation and serves as the lower confining zone, with an average thickness of 82 m [19]. The base of the Broom Creek Formation is approximately 1500 m above the Precambrian basement.

The Deadwood Formation unconformably overlies the Precambrian of the Williston Basin and consists of siliciclastics, carbonates, and evaporites. The Deadwood can be divided into six members, A–F [20]. The earliest Member A is Cambrian, composed of alluvially deposited conglomerates and sandstones. Member B consists of glauconitic shallow marine sandstones and siltstones. Members C–F consist of a lower Ordovician succession of three regressive–transgressive sequences containing sandstones, siltstones, mudstones, and carbonates. Members A–E are present in the study area. The Winnipeg Group unconformably overlies the Deadwood and consists of three formations: Black Island, Icebox, and Roughlock. The Black Island Formation is a mixture of sandstone and shale deposited in a fluvial–deltaic to shallow marine environment [21]. The Icebox Formation conformably overlies the Black Island Formation. The Icebox is a marine shale that serves as the primary upper confining zone, with an average thickness of 36 m. The Roughlock is a calcareous shale to argillaceous limestone. The continuous shales of the Deadwood Formation B member serve as the lower confining zone, with an average thickness of 10 m. In addition to the Icebox Formation, there are 174 m of impermeable rock formations between the Black Island Formation and the next overlying porous zone, the Red River Formation [19].

2.1.1. CSEM Feasibility Study

Injection of supercritical CO₂ into brine-filled reservoir rocks reduces the electrical conductivity and potentially produces a 4D anomaly that can be measured from the surface. We selected the CSEM method for CO₂ monitoring because it showed the strongest coupling to resistive and conductive formations [22,23]. A feasibility study was performed to determine the effectiveness of CSEM monitoring CO₂ injected into the Broom Creek and Deadwood formations [24]. Although the ultimate proof will be the three-dimensional time-lapse image from potential repeat surveys, the feasibility study’s prediction was verified with the initial field data by comparing the model derived from the well logs with inversion results for the one-, two- and three-dimensional EM methods used in the project plus the three-dimensional anisotropic model from fitting the measurements of all CSEM components.

The goal of the 3D modeling [25] was to estimate the expected surface EM field response level caused by an increase in CO₂ saturation and determine whether signals of that magnitude could be detected in the field in the presence of observed noise levels. Moreover, the feasibility study defined survey parameters, such as station spacing along survey lines, to maximize signal levels from target formations.

Integrating surface and borehole data is an essential requirement derived from 3D modeling. Data integration is achieved by measuring between surface and borehole, calibrating the information with conventional well logs, and considering resistivity anisotropy [23]. This process reduces the risk of imaging false anomalies [26–29]. Hence, combining advances in acquisition hardware, imaging methods, 3D modeling, and workflow to integrate surface models with borehole measurements in a CO₂-monitoring scenario is paramount. High measurement accuracy and overall repeatability (better than 0.5%) are required in this scenario [15]. This includes everything from instruments, operations, location repeatability, and environmental issues (atmospheric, cultural, and geologic noise). The target

reservoir signal band must be well within the center of the entire system signal band to avoid deconvolution of potential system responses [22].

Figure 3 shows the CSEM feasibility workflow. The workflow's input data are seismic horizons from two 3D seismic data sets and well logs from the four wells (A, B, C, and D) in the study area. Borehole resistivity logs are considered ground truth. Using an equivalencing process [22,30] and 3D modeling based on physics, we built a 31-layer equivalent model (3D anisotropic) that honors the lithological boundary and the log [31].

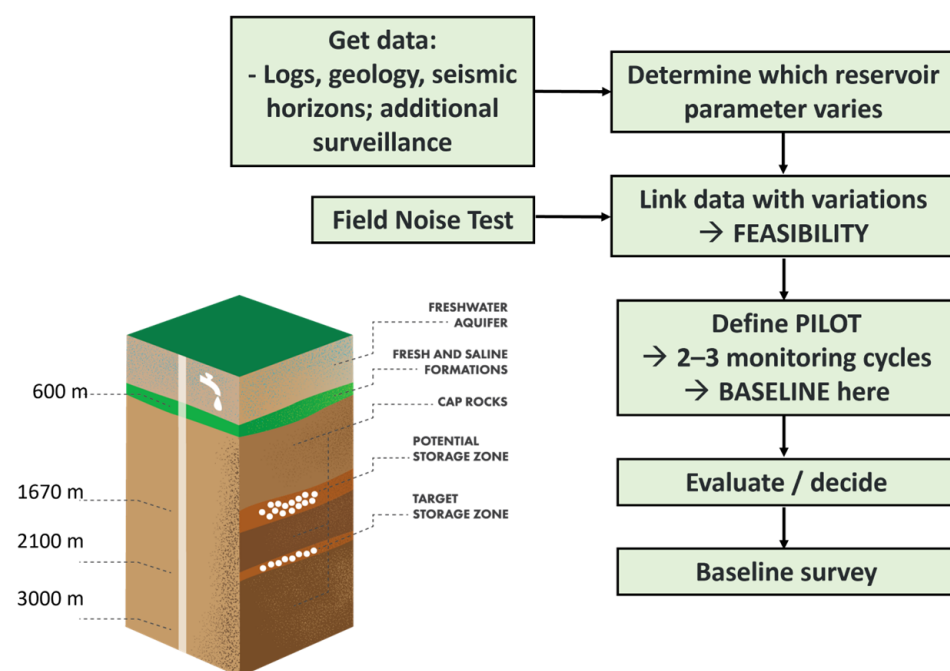


Figure 3. Feasibility workflow for CSEM fluid monitoring. The greatest modeling effort is in the feasibility step, which includes fluid substitution for various CO₂ and water saturations.

Rock physics is an essential element of the feasibility workflow, which provides the means to connect rock properties and fluid saturation determined from geology or petrophysics with measurements from geophysics. Rock physics can be used to predict how changes to rock properties and fluid saturation will affect the geophysical measurements and, thus, the feasibility of using geophysics to monitor the storage and sequestration of CO₂.

The geological data used in the rock physics analysis consist of regional geology, core descriptions from whole cores and thin sections, and core plug analysis results, including X-ray diffraction (XRD), X-ray fluorescence (XRF), and measurements of porosity, permeability, and grain density. Petrophysical data were corrected for tool and borehole effects and checked for consistency between wells. The volumes of the dominant minerals were used to determine the rock properties used in rock physics modeling. Lithology volume logs in the Broom Creek and Deadwood formations at each well were generated from the well logs using the TechLog Quanti.Elan module. The normalized solid volume results are shown in Figures 4 and 5. The results were quality-controlled, comparing the predicted volume fractions and porosities with the weight fractions from core XRD and core porosities.

The results show that the Broom Creek Formation's dominant lithologies are quartz, dolomite, and anhydrite. The Deadwood Formation's dominant lithologies are quartz and carbonate, with smaller volumes of clay and feldspar.

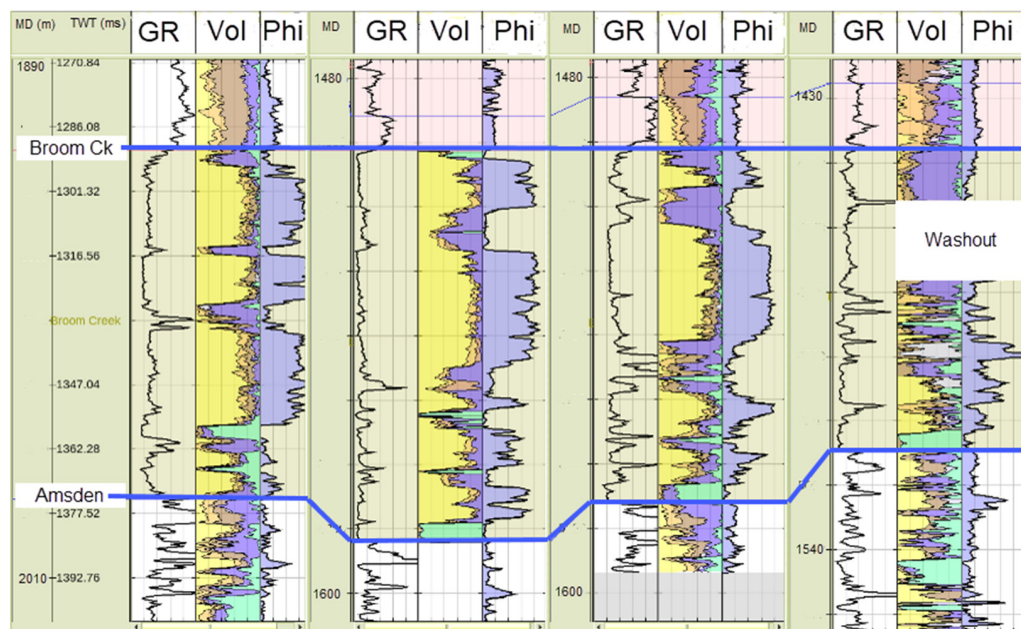


Figure 4. Q-ELAN lithology logs from the Broom Creek Formation. The wells from left to right are A, B, C, and D. The logs for each well, left to right, are environmentally corrected gamma ray, normalized lithologic volume (0–1), and porosity (0–0.4). The volumes were normalized and color-coded as anhydrite (green), dolomite (dark blue), calcite (light blue), quartz (yellow), clay (pink), and feldspar (light brown).

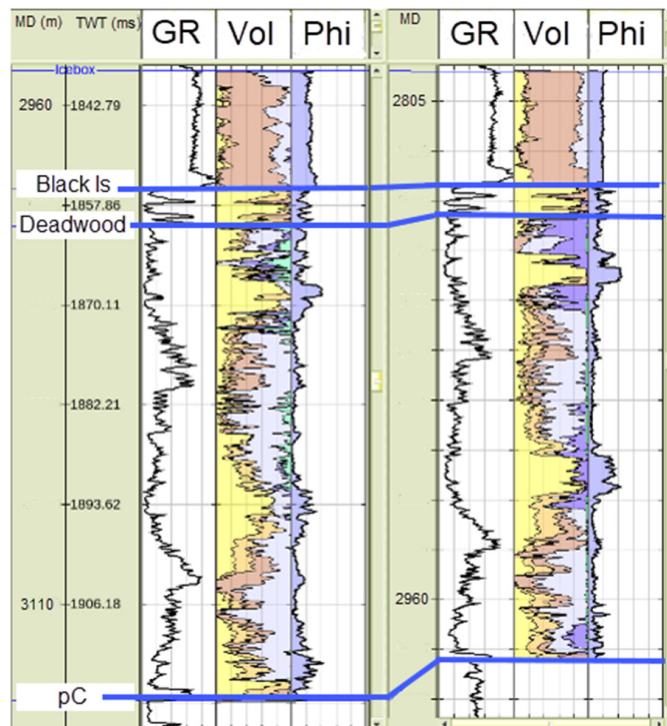


Figure 5. Q-ELAN lithology logs from the Deadwood Formation. The wells from left to right are B and D. The logs for each well, left to right, are environmentally corrected gamma ray, normalized lithologic volume (0–1), and porosity (0–0.4). The volumes are normalized and color-coded as anhydrite (green), dolomite (dark blue), calcite (light blue), quartz (yellow), clay (pink), and feldspar (light brown).

The lithology volume logs were used to calculate density porosity and composite rock grain elastic properties for rock physics analysis. Porosity logs were used to model rock properties and fluid substitution. The porosity logs should be consistent with core measurements and geologically consistent between wells. Density porosity or phid [32] was calculated from the density log using the lithology volume logs and formation brine densities from the Broom Creek and Deadwood formations.

The crossplot analysis of Broom Creek (Figure 6) based on wells A and C shows a complex formation dominated by a mixture of sand, dolomite, and anhydrite. The three-mineral mixture allows us to use a ternary plot to describe mineral composition. The sample points can be colored using a blend of red (sand), green (carbonate), and blue (anhydrite) in proportion to their rock compositions (Figure 6a). For crossplot analysis, sand is defined as the sum of quartz and feldspar, and carbonate as the sum of calcite and dolomite. The ternary plot and crossplot are connected by applying the color blends as the z-values in the crossplot, creating an integrated plot with five dimensions of information. The P-wave velocity/S-wave velocity (V_p/V_s) ratio vs. acoustic impedance (AI) results in Figure 6b indicate that sand has a low AI and high V_p/V_s ratio. In contrast, carbonates have a higher AI and lower V_p/V_s ratio. Anhydrite has the highest AI.

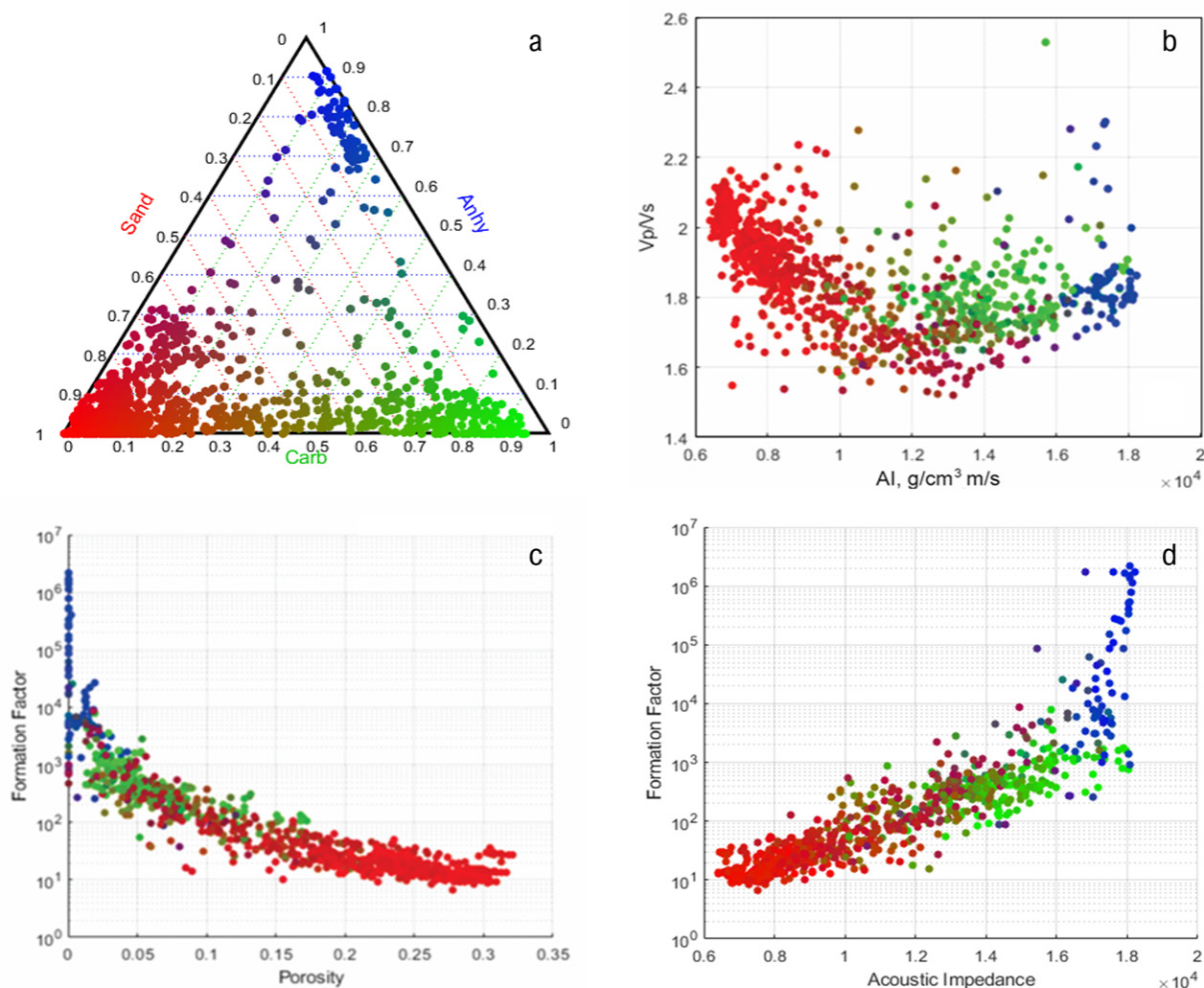


Figure 6. Broom Creek Formation ternary crossplot (a). The crossplots are (b) V_p/V_s ratio vs. AI, (c) formation factor vs. phid, and (d) formation factor vs. AI. The red–green–blue blended colors stand for the relative volumes of sand (red), carbonate (green), and anhydrite (blue).

The B and D wells were used for the crossplot analysis of the Deadwood Formation (Figure 7). The Deadwood Formation is a complex formation dominated by a mixture of sand (quartz + feldspar), carbonate (calcite + dolomite), and clay, which were used to create a ternary crossplot of mineral composition and rock physics properties. In the ternary plot (Figure 7a), mineral proportions are colored by mixing red (sand), green (carbonate), and blue (clay) in proportion to their volumes. The color is used to color the ternary plot and the samples (z-axis) of the crossplot. The results in Figure 7b indicate that sand is characterized by low AI and low Vp/Vs ratio, while the clays have a low AI and high Vp/Vs ratio. The carbonates have high AI and intermediate Vp/Vs ratios.

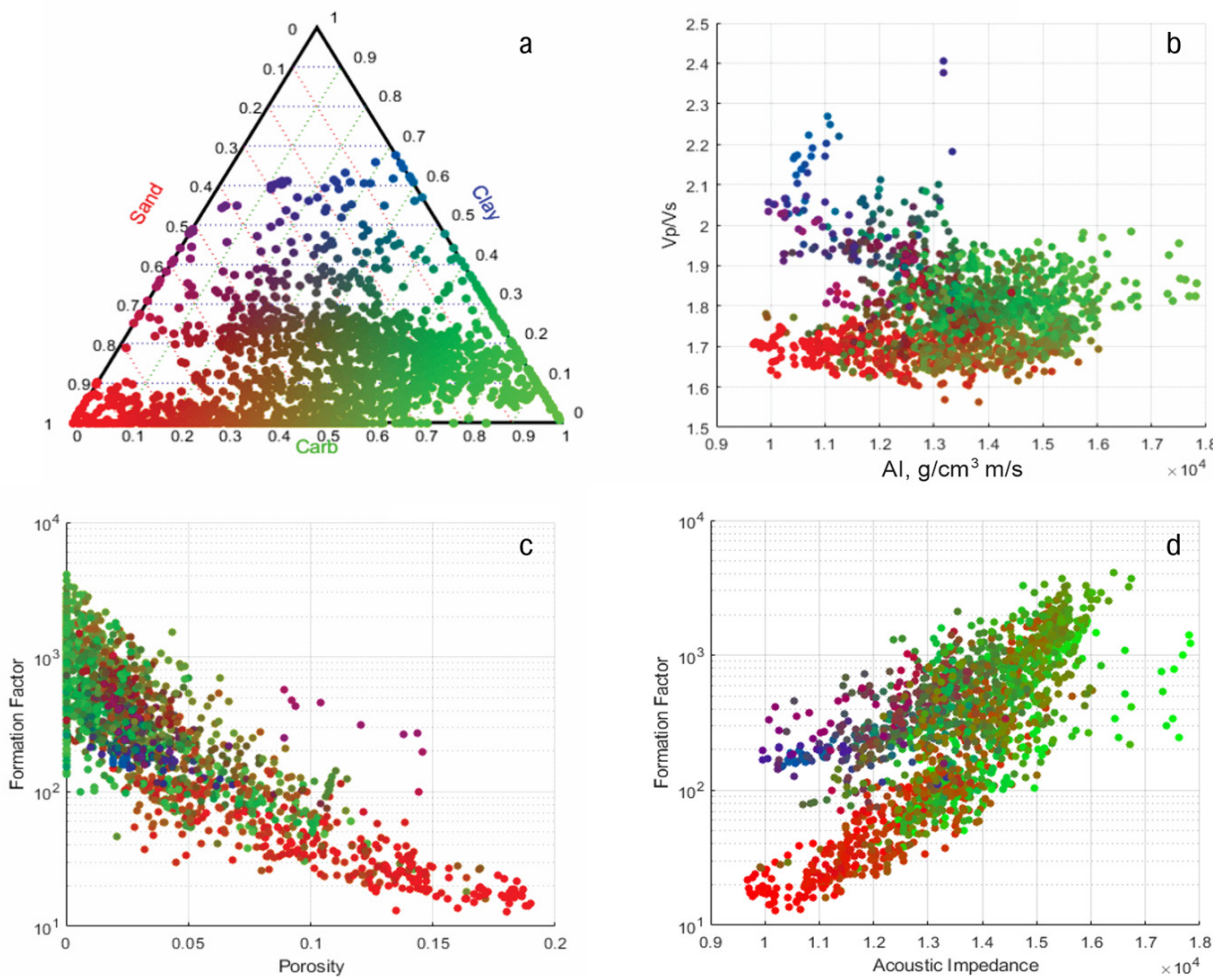


Figure 7. Deadwood Formation ternary crossplot (a). The crossplots are (b) V_p/V_s ratio vs. AI, (c) formation factor vs. phid, and (d) formation factor vs. AI. The red–green–blue blended colors stand for the relative volumes of sand (red), carbonate (green), and clay (blue).

Variations in rock physics properties can be linked with changes in geologic facies. The changes in composition, porosity, sorting, and diagenesis change the formation's elastic, density, and electrical properties. The geologic facies were found using the Heterogeneous Rock Analysis® (HRA®) module in Techlog®. In Broom Creek, HRA was used to define five rock types. The inputs to the facies analysis included triple-combo (tool string designed to measure formation density, porosity, deep/intermediate/shallow resistivity, natural gamma, radiation, hole size, and fluid temperature) and NMR wireline logs. The facies were characterized based on core data, including thin sections, XRD, and XRF. The results of the facies relationship to rock physics properties are shown in the V_p vs. phid crossplot

in Figure 8. The sandstone facies have high porosity and Vp, and anhydrite have low porosity and high Vp.

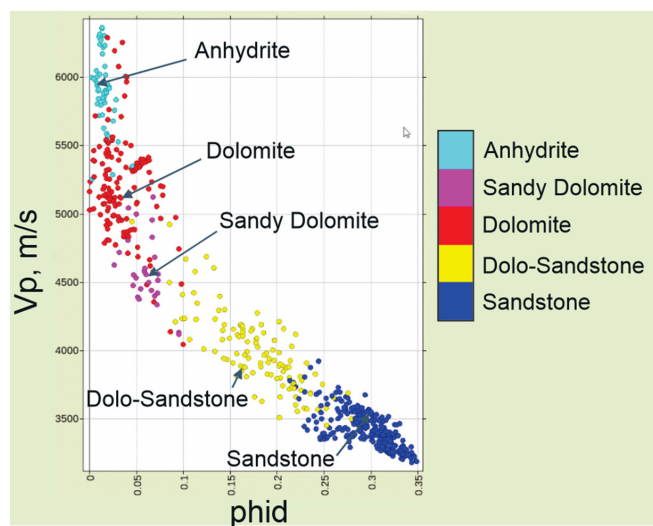


Figure 8. Vp vs. density porosity crossplot from B well based on the HRA facies analysis of the Broom Creek Formation. The HRA classification included five rock types.

The Deadwood–Black Island lithologies identified from Techlog Quanti.Elan inversion were used in a Vp/Vs vs. AI rock physics crossplot, as depicted in Figure 9, to identify facies trends for rock physics analysis. The polygons were created by applying lithology cutoffs to the data and then creating polygons to group the points. The lithology cutoffs used for the crossplot are sand ≥ 0.64 and illite, calcite, and dolomite each ≥ 0.36 by volume. Density porosity > 0.1 was also identified. The polygons show that the high porosities are associated with sand and that calcite and dolomite overlap and could be merged to form carbonate facies.

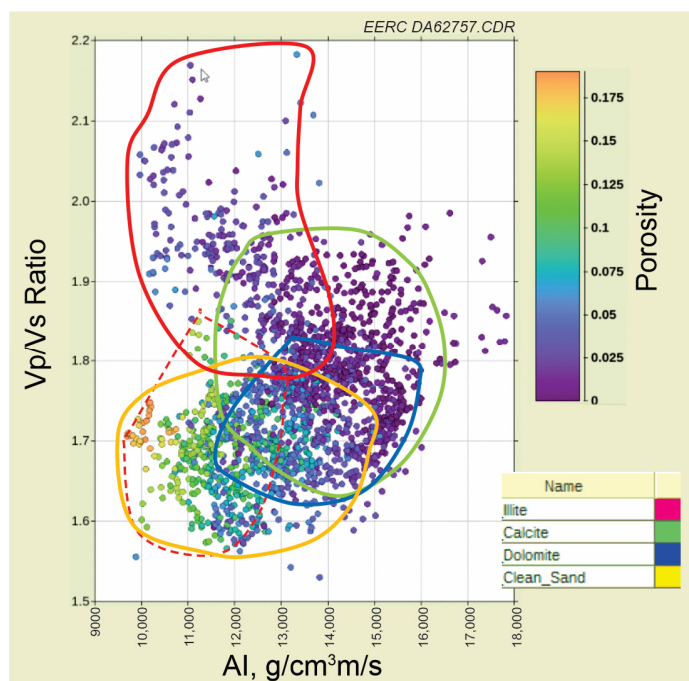


Figure 9. Deadwood rock-physics-based facies identification. Polygons: illite > 0.36 is red, calcite > 0.36 is light green, dolomite > 0.36 is blue, and sand > 0.64 is orange by volume. Density porosity > 0.10 is dashed red.

Fluid Elastic Properties

The fluids in the pore space affect the rocks' effective elastic and electrical properties. In general, liquids have higher density and bulk modulus than gases. Two fluids, brine, and CO₂ are expected to be present in Broom Creek and Deadwood during sequestration. The brine in Broom Creek is assumed to have a salinity of 64,100 ppm NaCl equivalent based on a sample from the Broom Creek Formation in the C well.

The properties of CO₂ are dependent on the pressure and temperature of the reservoir. The Broom Creek Formation in the study area has a temperature and pore pressure of 58 °C and 17 MPa. When the temperature and pressure are above 31 °C and 7.3773 MPa, CO₂ is in a supercritical phase. In this state, CO₂ has a liquid's density and a gas's bulk modulus. The elastic properties in Table 1 were calculated at Broom Creek reservoir conditions. Brine properties were calculated with the FLAG calculator [33] built into RokDoc. The properties of dry CO₂ at reservoir conditions were calculated by the NIST CO₂ property calculator [34].

A small amount of CO₂ will dissolve into the brine to produce a CO₂-saturated brine [35]. Han and Sun [36] measured the density and Vp of CO₂-water mixtures at typical reservoir temperatures and pressures. These authors produced empirical equations to predict the bulk modulus and density of CO₂-saturated brine. Their equations were used to approximate the properties of CO₂-saturated brine in the Broom Creek Formation. The CO₂-saturated brine has a saturation of 27.6 L/L at standard temperature and pressure conditions of 15.56 °C and 0.10133 MPa. The results are given in Table 1. Alternative property estimates for CO₂-saturated brine can be found in the literature, including [35,37].

The Deadwood Formation in the study area has a temperature and pore pressure of 83 °C and 31.7 MPa. Any CO₂ injected into it will be supercritical. The bulk modulus and density of the fluids in the Deadwood pore space affect the effective elastic properties sensed by the seismic data. The elastic properties of the fluids at reservoir conditions are given in Table 2. Based on the fluid properties, free CO₂ in the reservoir will reduce the effective density and Vp of the reservoir and, depending on the rock's stiffness, may produce a contrast with the brine-filled reservoir. A small amount of CO₂ is expected to dissolve into the brine, with a maximum saturation of 17.3 L/L at standard conditions.

Fluid mixing of CO₂ and brine can vary between homogeneous and heterogeneous. In the reservoir, CO₂ and brine will mix at all scales, where the amount of mixing depends on reservoir properties [38] and the engineering characteristics of the injection process [39]. If the reservoir is in capillary equilibrium, the brine and CO₂ saturation distribution will be controlled by capillary pressure curves associated with various geologic facies. Since capillary pressure is significantly influenced by permeability, variation of reservoir permeability has a significant role in saturation distribution [38]. Adams et al. [40] and Barajas-Olalde et al. [41] published in-depth rock physics studies of the Broom Creek and Deadwood formations for seismic CO₂ monitoring in the study area.

Electromagnetic Properties

The conductivity of the minerals and fluids in the formation and the conductivity of the drilling mud affect electrical resistivity or conductivity logs. In the Broom Creek Formation, brine resistivities were measured in the A, B, and C wells. Fluid replacement modeling using Archie's equation [42] was used to normalize the electrical conductivity and formation factors of the A, C, and D wells to the B well. The original electrical conductivity is shown in Figure 10a, and the final conductivity after substitution is shown in Figure 10b. The electrical conductivities were more consistent after fluid replacement.

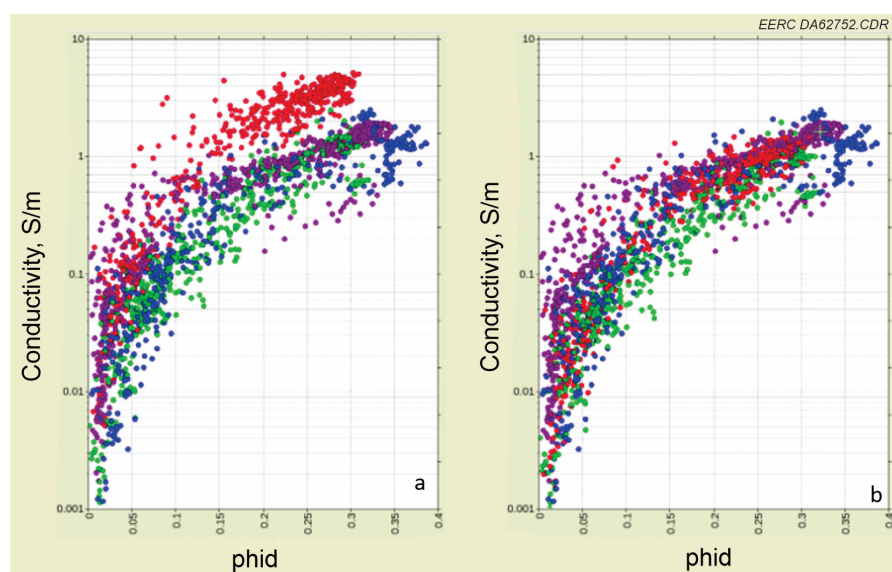


Figure 10. Broom Creek Formation electrical conductivity vs. porosity (a) before fluid substitution and (b) after fluid substitution to a common brine salinity. The data are colored by A (red), B (purple), C (green), and D (blue) wells.

Deadwood brine salinity was measured only in the B well. Initially, the measurement was used for both wells (see Figure 11a). The sample distributions for the B and D wells were inconsistent. A consistent result was obtained after adjusting the D fluid resistivity ($R_w = 0.0375 \text{ ohm-m}$), as shown in Figure 11b. The mud filtrate's resistivity (R_m) in the D well was 0.0329 ohm-m at 83°C , which suggests that mud filtrate is a significant factor in the D resistivity readings.

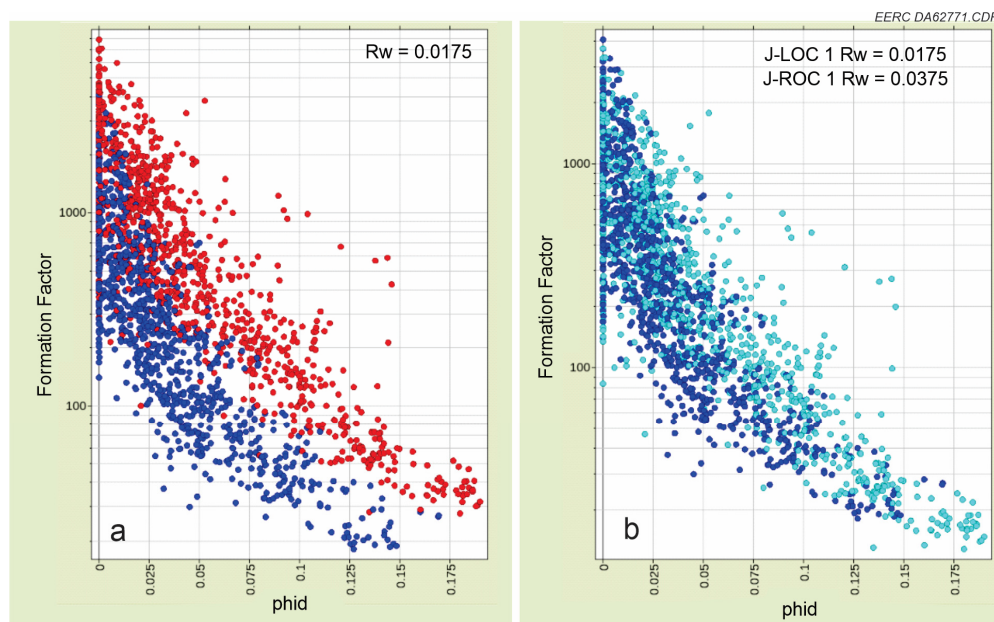


Figure 11. Deadwood Formation factor vs. porosity. (a): The measurements are color-coded by well where B is blue and D is red. (b): The measurements are color-coded by well where D is light blue and B is blue. The left panel is before correction using $R_w = 0.0175 \text{ ohm-m}$ from the B well. The right panel is after correction using $R_w = 0.0175 \text{ ohm-m}$ from the B well brine salinity and $R_w = 0.0375 \text{ ohm-m}$ in the D well.

Rock Electrical Properties

Most common rock-forming minerals, except for clay, are insulators at the frequencies used in geophysics. Under these conditions, the electrical conductivity of the formation is determined by the electrical conductivity of the brine and the porosity/permeability of the rock [43]. Formation factor [42] provides a way of normalizing resistivity or conductivity logs for the influence of changes in brine resistivity between wells.

Ternary crossplots were also used to examine the relationship between the Broom Creek and Deadwood Formations' porosity, lithology, and formation factor, as shown in Figures 6c and 7c, respectively. In Figure 6c, the lowest formation factors (10–100) of the Broom Creek Formation are associated with high-porosity (>0.15) sand, while carbonate is low-to-medium porosity (0.02–0.15) and has intermediate formation factors (100–2000). Anhydrite is associated with the lowest porosity (<0.05) and the highest formation factors (>2000). For the Deadwood Formation (Figure 7c), the distribution is continuous where the lowest formation factors (10–30) are associated with high-porosity (>0.15) sand, the highest formation factors (>200) are associated with low-porosity carbonate (<0.05), and clay is related to low porosity (<0.07) and intermediate formation factors (100–200).

The electrical and elastic properties of a rock have no common fundamental physics properties. However, as shown for Broom Creek in Figure 6d and Deadwood in Figure 7d when cross-plotted, they show significant correlation. The cleanest sands are associated with low acoustic impedance and formation factor; increasing the volume of carbonate causes both properties to increase. The connection creating the correlation is an arrangement of the minerals in the rock. Correlations like this suggest that electromagnetic and seismic methods provide complementary information about the reservoir.

Fluid Electrical Properties

The Broom Creek electrical resistivity in Table 1 was determined from Schlumberger well log interpretation tables [44]. Supercritical CO₂ is assumed to be an insulator. The authors of [45] cite a value of 1×10^{-8} S/m in their review paper. The CO₂-saturated brine in the Broom Creek Formation is expected to have a saturation of 27.6 L/L CO₂ at standard conditions. Using the equations given by [13], CO₂-saturated brine is expected to have 0.9 of the conductivity of the original brine.

The brine salinity 256,000 ppm NaCl equivalent in the Deadwood Formation was determined from a sample acquired in the B well. The D brine was assumed to have the same salinity. Supercritical CO₂ is assumed to be an insulator. A small volume of CO₂ can enter into a solution with brine. In the Deadwood Formation, the saturation is expected to be 17.3 L/L CO₂ at standard conditions. The electrical conductivities of the three fluid phases are given in Table 2. CO₂-saturated brine had an electrical conductivity of 0.93 of the brine. Given various CO₂ saturation levels, many 3D models were calculated for the feasibility study.

Table 1. Broom Creek Formation elastic and electric fluid properties.

| Fluid | T (°C) | P (MPa) | Density (kg/m ³) | V _p (m/s) | K (GPa) | σ (S/m) | Boerner Coefficient | Elastic Reference | Electrical Reference |
|----------------------------------|--------|---------|------------------------------|----------------------|---------|---------|---------------------|-------------------|----------------------|
| Brine | 58 | 17 | 1035 | 1642 | 2.791 | 15.38 | NA * | [33] ¹ | [44] |
| CO ₂ | 58 | 17 | 681 | 365 | 0.091 | 0 | NA | [34] ² | Assumed |
| CO ₂ -Saturated Brine | 58 | 17 | 1043 | 1637 | 2.797 | 13.79 | 0.8963 | [36] | [13] |

¹ RokDoc FLAG fluid property calculator [33]. ² National Institute of Standards and Technology CO₂ property calculator [34]. * Not applicable.

Table 2. Deadwood Formation elastic and electrical fluid properties.

| Fluid | T (°C) | P (MPa) | Density (kg/m³) | Vp (m/s) | K (GPa) | σ (S/m) | Boerner Coefficient | Elastic Reference | Electrical Reference |
|----------------------------------|--------|---------|-----------------|----------|---------|----------------|---------------------|-------------------|----------------------|
| Brine | 83 | 31.7 | 1168 | 1816 | 3.852 | 57.14 | NA * | [33] ¹ | [44] |
| CO ₂ | 83 | 31.7 | 750 | 488 | 0.179 | 0 | NA | [34] ² | Assumed |
| CO ₂ -Saturated Brine | 83 | 31.7 | 1176 | 1811 | 2.86 | 52.98 | 0.9272 | [36] | [13] |

¹ RokDoc FLAG fluid property calculator [33]. ² National Institute of Standards and Technology CO₂ property calculator [34]. * Not applicable.

CSEM 3D Modeling

The CSEM setup includes a transmitter and receiver moved along profile lines, as shown in Figure 12. The survey layout consists of three lines of receivers and two separate CSEM transmitter sources to the north and south of these lines. We chose two transmitters to see and account for larger directional structural changes and anisotropy effects. More details on the hardware can be found in Strack et al. [15]. Each transmitter had two dipoles in perpendicular directions to account for local anisotropy variations. The log was scaled to 32 layers with anisotropic resistivities shown superimposed on the log on the right of Figure 12. The upscaling was verified with 3D modeling within 1%, and seismic and lithologic boundaries were maintained. The upscaled log represents the ground truth for CSEM based on the well logs.

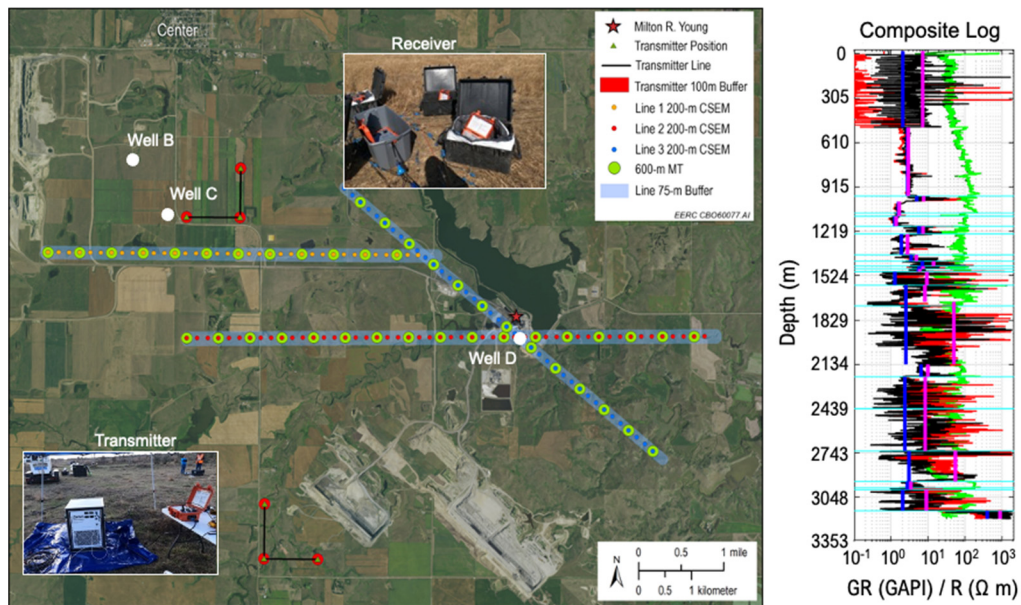


Figure 12. CSEM and MT survey layout and composite log used in the feasibility study. CSEM receivers were placed at 200 m intervals (small red, orange, and blue dots) along the three shaded lines, and sources were placed at two transmitter sites. MT sites were deployed at 600 m intervals along the receiver lines, indicated by the large green dots. The white dots represent the location of wells B, C, and D (the map does not cover the location of well A). The big red circles and black lines represent the transmitters. Exemplary equipment images are also shown. To the right is the composite resistivity log, and superimposed is the upscaled log with 31 layers shown with vertical (magenta) and horizontal (blue) resistivities. The light blue lines represent seismic reflection horizons that were kept fixed along with lithological boundaries.

For the 3D modeling, one transmitter and fourteen receivers along the three-receiver lines were used to build various 3D modeling tests. In the field, 13 receivers were moved

along the profile lines. The receivers were at the injection well and represent the most distant receivers from Transmitter Location 1 (north location in the study area) and serve as a reference. All electromagnetic field responses and the time changes were modeled. An exemplary display is shown in Figure 13 for the Broom Creek Formation. These models were also used to estimate the optimum parameter range. Here, the results are displayed in the context of defining the optimum station spacing by displaying the 100 m, 200 m, and 300 m site spacing. The curve colors correspond to the site locations shown at the bottom of the figure, along with the chosen injection plume radius. Note that the plume radius can be seen on all curves.

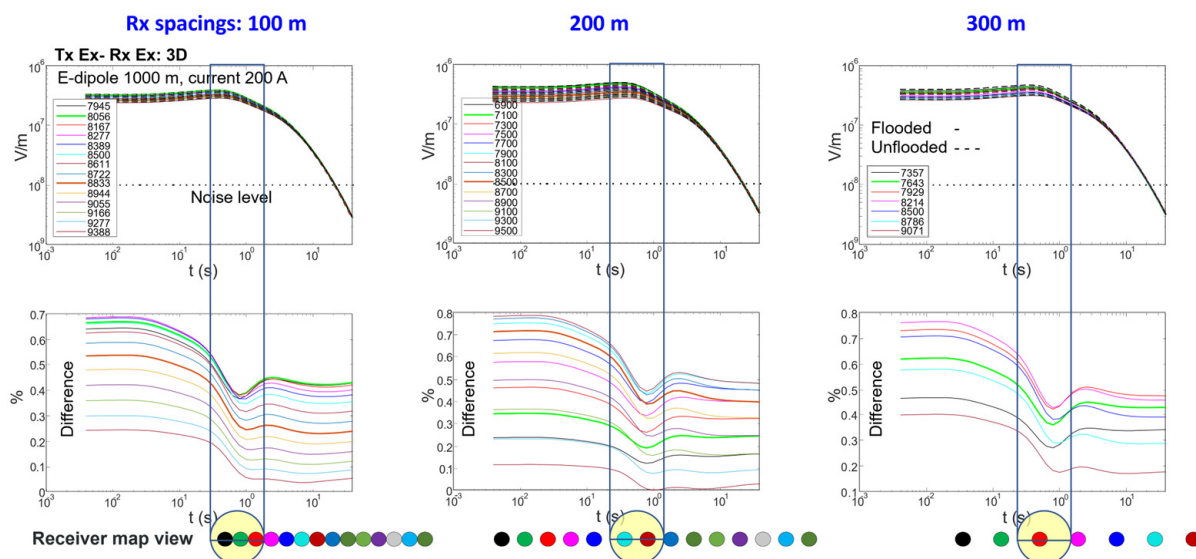


Figure 13. Example of 3D modeling results for various offsets (meters) between transmitter and receiver for different receiver station spacings.

Furthermore, the curves can be interpolated from the left to the right. The largest total amplitude in the electric field values can be seen for the 200 m spacing, which is why this was chosen for the survey. All other components behaved similarly. The benchmark models covering most field scenarios were based on petrophysical analysis. Then, the equipment/sensor choice was added to the 3D modeling results. The result is a set of models including the expected anomaly within the measurable time window.

Twenty-one months of CO₂ injection in the Broom Creek Formation was simulated using a 60% average CO₂ saturation and an injection radius of 500 m. The simulation showed that 15–18 months of injection produced a strong anomaly. Next, an injection radius of 150 m was used, and the required receiver spacing was estimated. Figure 13 depicts the 3D modeling results for the Broom Creek Formation for Ex (Ey and dBz/dt are not shown here). The reference noise from the noise test is shown at each component (horizontal dotted line). The response of all the components is above the noise level. The curve variations between the three spacings are smooth; therefore, the CO₂ anomaly can be reconstructed for 100 m, 200 m, and 300 m receiver spacings.

As the Deadwood Formation has lower porosity and is significantly deeper than the Broom Creek Formation, a conservative 30% CO₂ saturation after injection (representing a 150 m flood zone radius) was considered. The responses and differences corresponding to reservoir conditions before and after CO₂ injection were between 1% and 5% for a 1D model and below 1% for 3D models. Based on these results, monitoring injected CO₂ in the Deadwood Formation under the assumed field and survey parameters will be challenging, and novel anomaly-enhancing methods will be needed.

Field Noise Test

Concurrent with the 3D modeling, field measurements were conducted near the potential injection plant to assess noise conditions. This allows optimization of the survey design and estimation of the data's signal-to-noise ratios. Magnetic field sensors, electric sensors, and recording units were used in the test. An example of the amplitude spectra of the noise measurements is shown in Figure 14. The amplitude of the noise recorded by the induction coils was higher than the air coil's noise. This difference suggests that the areal averaging of the air coil reduces some of the localized noise (we did not see the same at different survey sites). The 60 Hz noise and its harmonics observed in the raw data were attenuated as part of the data acquisition/processing. Subsequently, the receiver data were used to simulate noise combined with the transmission cycle and signal processing. A CSEM transmitter's response was modeled for four transmitter-to-receiver offsets used in the field using the 31-layer anisotropic model. The analysis shown yields stacked data as an excellent noise-level estimator on the right of Figure 14. The resulting estimated optimum recording for CSEM data acquisition is 3:40 h. This proved very useful during the 24-rotation acquisition (a minimum of 4 h of recording time was used depending on local noise conditions and real-time quality assurance).

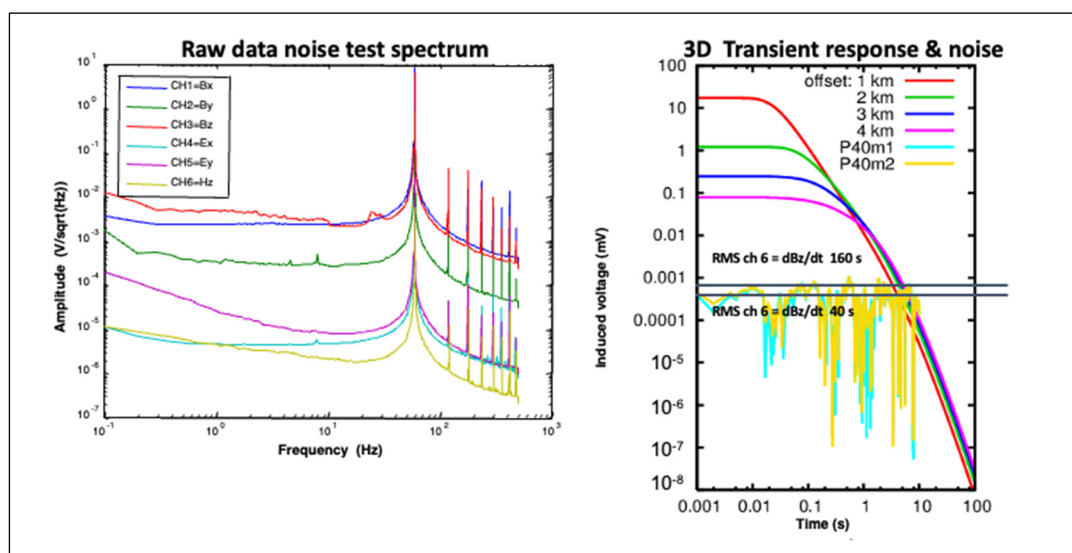


Figure 14. Summary of the noise test and results compared with the 3D modeling responses. The top left shows the power spectra. The power spectra for two different acquisition settings, m1 and m2, and the 3D modeling responses for four offsets are displayed on the right. Two power spectra use different recording times. The black horizontal lines mark the average noise level for magnetic field sensors.

For the MT acquisition, the skin depth formula and the estimated lowest frequency at approximately 3000 m deep were used to derive the recording time for the MT data acquisition. The high frequency (HF) range includes power line noise and uses HF data processing, and the low frequency (LF) range is below the power line noise and uses LF data processing (all robust processing). This range was used for overnight data acquisition. The duration variation depended on when the station setup was finished and when the station was moved the next day.

2.1.2. CSEM and MT Data Acquisition

Based on these feasibility study results, a time-lapse CSEM monitoring project was designed. The survey layout and design are shown in Figure 12. The baseline survey was taken before the CO₂ injection into the formations. Furthermore, an MT survey was performed in conjunction with the baseline CSEM survey to measure field site background

resistivity. The survey was carefully designed, and special attention was paid to noise levels in the field to ensure that any time-lapse differences observed would be solely due to changes in CO₂ concentration within the reservoir. All acquisition hardware was carefully controlled for variations and calibrations were conducted before, during, and after the survey. Long-term stability was shown to be better than 0.5% in the worst case (1 out of 14 instruments).

The initial EM surveying lines were designed to overlap the 2D seismic lines recorded in the study area. Protected areas were avoided when setting out the lines, and most stations were located at least 100 m away from power lines to avoid disturbance from EM noise. The survey layout consisted of three lines of receivers and two separate CSEM transmitter sources to the north and south, each with two dipoles. Given the optimal 200 m station spacing as determined from the feasibility study, 125 CSEM receiver locations were used. The receivers consisted of 100 m long dipoles oriented north–south (Ex) and east–west (Ey). An air loop or buried induction coil was laid out on the northwest quadrant of each receiver site to measure the vertical magnetic field (Hz). Contact resistance was logged at each site for quality assurance during acquisition, processing, and interpretation.

CSEM in the time domain was selected for this project because of its high sensitivity in onshore applications (e.g., [15,46–48]). CSEM with grounded electric dipole excitation is better suited for reservoir analysis since the grounded transmitter excites horizontal and vertical currents in the formation, making the method sensitive to thin anisotropic resistors. However, in CO₂ monitoring, sensitivity to both resistors and conductors is needed; namely, a full 3D anisotropic model [23].

Each source consisted of buried electrodes connected by a 1 km cable to the transmitter. The transmitter was set to transmit between 160 and 250 amperes of current. The actual current was monitored and recorded during transmission to normalize the data. The recording times for each receiver station were between 4 and 5 h. Extended long recording times (total of 7 h per transmitter) were conducted at overlapping sites for use as reference locations should later time-lapse processing require this.

The total frequency range of MT data can be from 40 kHz to less than 0.0001 Hz, depending on the equipment used (here, we mainly used up to 1 kHz and sometimes up to 20 kHz). The ratio of the electric (Ex, Ey) and magnetic (Hx and Hy) recorded values gives an estimate of the apparent resistivity of the Earth at different depths. This estimate can be used to differentiate between rocks with contrasting resistivities, such as sandstones saturated with brine, and those where CO₂ has been injected.

Forty-two MT site locations were deployed, as depicted by large green dots in Figure 12, with a spacing of 600 m between each MT recording site. Three planned stations near the power plant were skipped during the survey because of noise/access issues. Six additional sites were located close to a noise source; the recorded data were reviewed in these cases, and the measurements were repeated because of unsatisfactory quality. A primary remote reference site was in Grand Forks, North Dakota, and a backup site was operated in Austin, Texas. MT data quality was greatly improved by using the remote reference during data processing.

Quality Assurance/Quality Control

Quality assurance/quality control (QA/QC) procedures were performed both in the field during collection and after data processing. Additional measures were considered when the receiver sites were in relatively high EM noise areas, including carefully selecting the appropriate electric line length when laying out the site, extending data acquisition time, and conducting necessary repetitions based on closely monitoring daily operations.

For MT measurements, the data were uploaded to the Cloud, and results were returned the following day, including remote reference processing where available. An example is given in Figure 15. The single site processing on the left still shows a mismatch between data (circles) and the inversion model response (line). This difference was caused by local

low-frequency noise, which was almost wholly removed when applying remote reference processing [49].

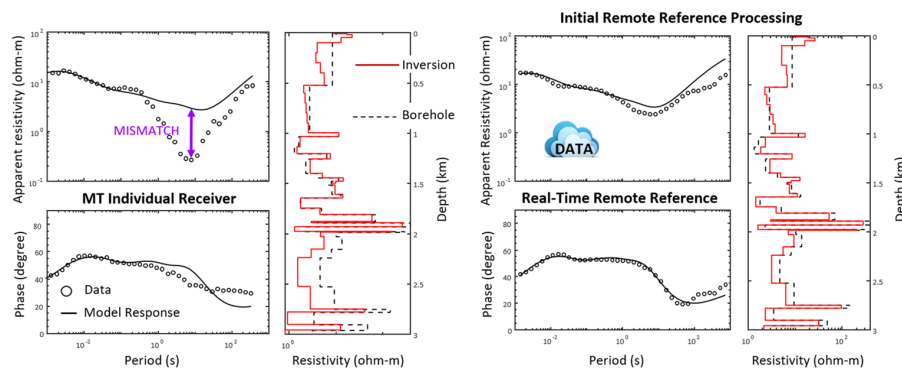


Figure 15. Example of the MT quality control. The data are sent from the receiver and remote reference site in the Cloud and returned in the morning. Overnight data are processed and inverted for a single site, as shown on the top left. The results are shown on the right after remote reference data have been applied (when available). The one-dimensional inversion results (red line) are compared with the borehole log (black line).

Figure 16 depicts the CSEM field workflow using cloud services for real-time data quality assessment. Data were uploaded to the Cloud for quality assessments during 24 h field operations. Since the inversion is based on electromagnetic fields, we only conducted quality assurance of the voltages. This also allowed us to QA the data without normalizing the transmitter current and operation parameters (time-consuming). If a receiver station showed poor data quality, the station was investigated, and the measurements were repeated until the quality improved. Examples of high-quality transmitter and receiver data are depicted in Figure 16. This workflow was fundamental to maintaining high data quality while monitoring acquisition equipment moved along the survey line (leapfrogging). High source/receiver repeatability was obtained, with an error difference of approximately 0.5%.

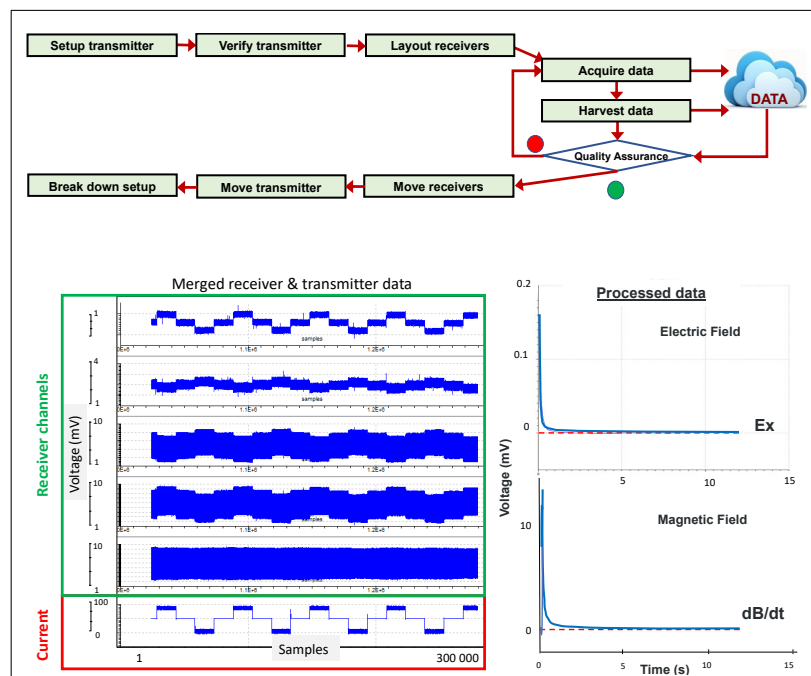


Figure 16. CSEM acquisition workflow (**top**) and data examples (**bottom**). The bottom left shows the merged raw receiver and transmitter time series. Stacked data for electric and magnetic fields are on the right.

CSEM and MT Data Processing

After passing initial QA during acquisition, transmitter and receiver data were merged into matching the transmitter–receiver pair files. This process also included time alignment between the transmitter signal and receiver data, a correction for time shifts, and the current waveform. Once all input parameters were verified (including onset time, transmitter current used for normalization, waveform period, and type of waveform), a three-point delay filter was applied to ensure waveform symmetry. Initially, we tested parameters with various other filters described in [22,48,50,51], but in the end, there were sufficient statistics that stacking rejected most noise.

For the MT data, we obtained an apparent resistivity and phase curve for each location that was of acceptable quality. This was carried out more carefully at the post-acquisition time with a more detailed analysis. Two-dimensional inversion was applied to the data to generate a resistivity model along the profile, as shown in the top part of Figure 17. These 2D models were the starting 3D resistivity model used for the 3D MT inversion, with an outstanding result shown at the top left and bottom of Figure 17. Notice the lateral and vertical resistivity variations in the profiles. These results reflect the MT method's sensitivity to the study's geologic conditions and the data quality.

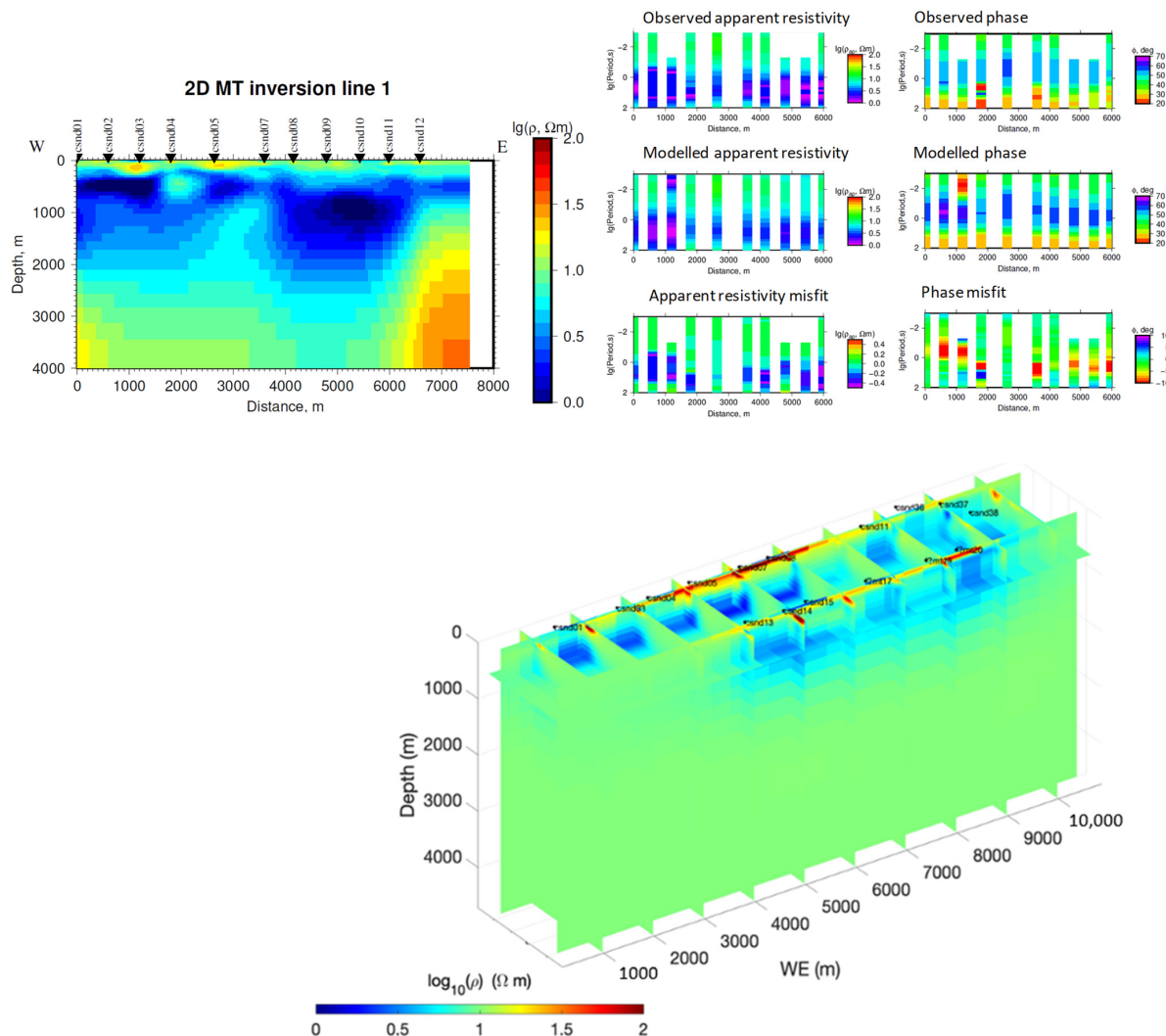


Figure 17. Two-dimensional (**top**) and three-dimensional (**bottom**) inversion results for MT data from the North Dakota CCUS survey. Three-dimensional inversion results are displayed with the viewpoint from the southwest.

In postprocessing, the time-series data were evaluated for data quality. The data were categorized as excellent, good, noisy (acceptable), or poor, depending on the pattern and rate of both magnetic and electric transient decay. All categories of data may additionally show transient reversals (zero crossovers), suggesting the possible presence of signal channeling or 3D structures. Because of the careful field data collection process, approximately 85% of the collected data were classified as good or excellent. Another 6% could be further processed to reach that level of quality. For a field CSEM data set this large, this is a high level of data retention and nicely sets up future time-lapse surveys for success. An unconstrained 1D inversion was performed for each receiver site, and the error bars from the stacking were used as data weights in the inversion. After paying careful attention to the distribution of the eigenvalues of the inversion model parameters, we removed more data restrictions and a priori constraints as the eigenvalues were statistically distributed, meaning the data were sensitive to 3000 m depth. The results were compared to an anisotropic borehole resistivity model to validate the data further.

Figure 18 compares the one-dimensional CSEM inversion to the two-dimensional MT inversion for Line 1 (northern E-W profile) and the three-dimensional modeling results, including the seismic horizons. The CSEM data in this inversion are from a representative site on the 2D MT inversion section. The borehole log is represented in black, while the CSEM inversion models and the anisotropy coefficient are in red and blue, respectively. It is worth noting that the inversion was performed unsupervised with a half space of 31 layers as the starting model. The inversion results match the log well. The panel on the right shows the comparison of the data with the 3D model response, including the log and adjusting the model depth by the seismic horizon depth at that site. The 3D model response on the figure on the right (dashed line) fits the data well in all components except for a later time in the Ex component when the signal disappears in noise, as this component is weaker due to transmitter symmetry consideration.

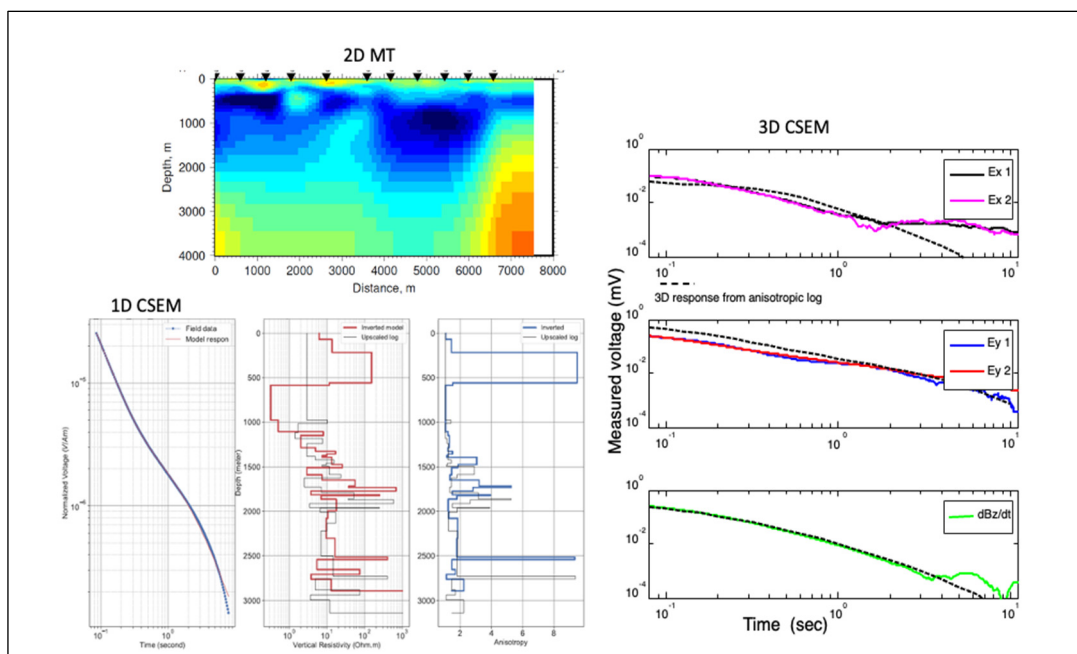


Figure 18. Comparative display between 2D MT inversion (Line 1) results (**top left**), an example of the 1D CSEM inversion (**bottom left**), and the 3D response model response and the CSEM field data (electric and magnetic components) for one site (**right**). The 1D CSEM panels represent (from left to right) the electric field in the transmitter direction Ex (dots: data; solid line: model response), inversion results (vertical resistivity and anisotropy coefficient, and superimposed 3D anisotropic log).

1D inversion results (in red) and the borehole model (in black) of eight sites adjacent to each other along Survey Line 2 and Transmitter 2 (south) are shown in Figure 19. Generally, inversion results align well with the borehole data, indicating high confidence levels in data collection and processing. The shaded outlines indicate the interpreted Broom Creek and Deadwood formations from the inversion results. Further results were validated by comparing the inverted resistivity models with 3D seismic data with the Broom.

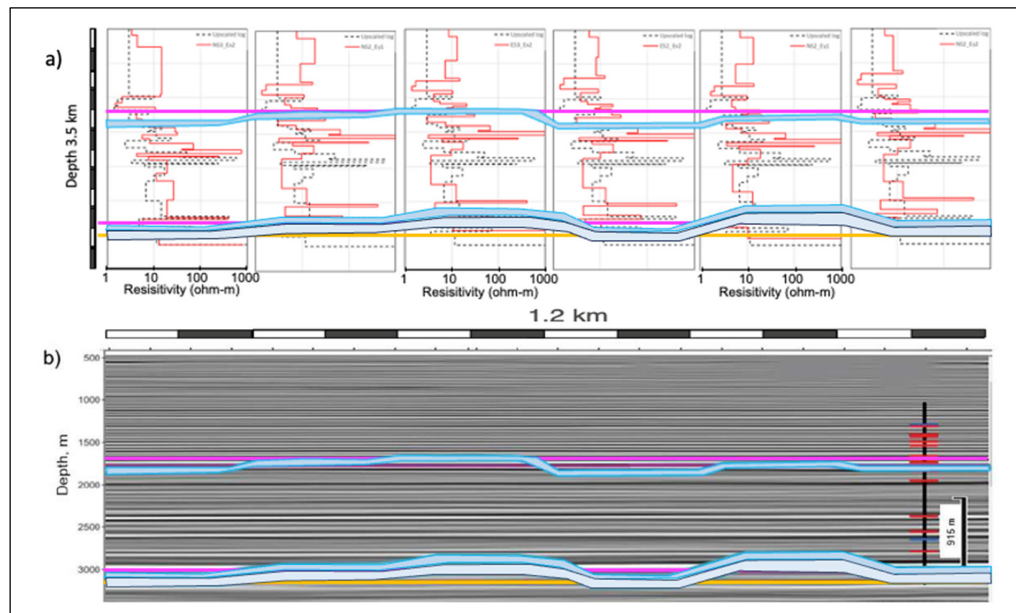


Figure 19. CSEM inversion results (a) (red) compared with the respective borehole reference model (black) for the 1200 m section of Line 2. The respective portion of seismic section (b) is plotted below. The Broom Creek and Deadwood formations are marked by the magenta line on the seismic section. The potential injection reservoirs are shaded.

Creek and Deadwood seismic horizons (in the bottom part of the figure). For most stations, the CSEM inversion accurately matches the seismic model. Inversion results that deviate from the seismic model could indicate lower data quality or denote areas of 3D structure unaccounted for in 1D inversion. Based on independent, unsupervised 1D inversions (starting model is a half-space), these results confirm the quality of the CSEM baseline measurements.

2.2. Geothermal

In 2021, global use of geothermal energy for thermal applications increased to approximately 141 terawatt hours (TWh), while direct use of geothermal heat reached about 128 TWh. However, the global distribution of geothermal energy use for power generation and heating/cooling remains sparse, with at least 82 percent concentrated in a few countries such as China, Turkey, Iceland, the USA, Japan, El Salvador, New Zealand, Kenya, and the Philippines [52,53]. With its vision for 2030, Saudi Arabia recognized and began diversifying its economy and reducing its reliance on fossil fuels. Therefore, developing renewable energy sources, including geothermal resources by 2030 and net zero carbon emissions by 2060 [54], is a top priority.

Geothermal resources in Saudi Arabia are promising. Several exploration campaigns and research studies have investigated Saudi Arabia's geothermal resources for decades [55–61], with a couple focusing on the Al-Lith area in southwestern Saudi Arabia [62–65]. The Al-Lith area has four hot springs with surface temperatures ranging from 41 °C to 96 °C, with Ain Al-Harrah having the highest. The Ain Al-Harrah hot spring's geothermal reservoir is characterized by a high surface temperature of up to 96 °C and favorable petro-thermal characteristics of 185 °C (reservoir temperature), 219 kJ/kg

(discharge enthalpy), and 183 mW/M^2 (heat flow) to provide long-term electricity to the Al-Lith area. Due to limited geophysical measurements in this area, these claims require further verification. We report here only the initial findings of the MT measurements, which are used to plan a more detailed CSEM survey later to drive future new drilling targets. Notice the primary targets for geothermal energy are conductive, while for CO_2 monitoring, the CO_2 plume is resistive. Therefore, MT plays a more critical role in geothermal energy than in CCUS. However, both cases require all EM components from the MT and CSEM methods to differentiate the fluid signature from the surrounding host rock.

Thirteen MT stations were collected using non-polarizable electrodes, and low-frequency induction coils. This data acquisition system used in a 40°C environment in Saudi Arabia is identical to the equipment used in the North Dakota CCUS example mentioned above at -20°C . The data were acquired for about 7 h at three different sampling frequencies of 4 kHz, 1 kHz, and 40 Hz. The raw data were processed in detail to ensure high-quality results. This stage involved a spectrum analysis and coherence to examine the relationship between two orthogonal and parallel fields. The impedance tensor was estimated using a robust statistical technique. The multiple impedance tensor results were further processed to extract the final transfer function data. Finally, the impedance tensors were inverted using a smoothness constraint algorithm for better image and interpretation.

The final 2D inverted section along the N-S profile (blue sites) in the study area is shown in Figure 20. The selected subset shows the flow and the reservoir best. The remaining data acquisition is ongoing and will be subject to a later complete analysis. The preliminary results of this MT study are the following:

- The geophysical survey detects and clearly maps the heat source, a low-resistivity hot body below a depth of 7 km.
- The geothermal flow cell observed at the bottom of the figure (hot fluids—green area) consists of the fractured basement acting as the pathway for the geothermal fluids to reach the surface.
- The heat exchanger is represented by the whole system, where the heat transfer consists of conduction through the hot body and convection via the flow cell.

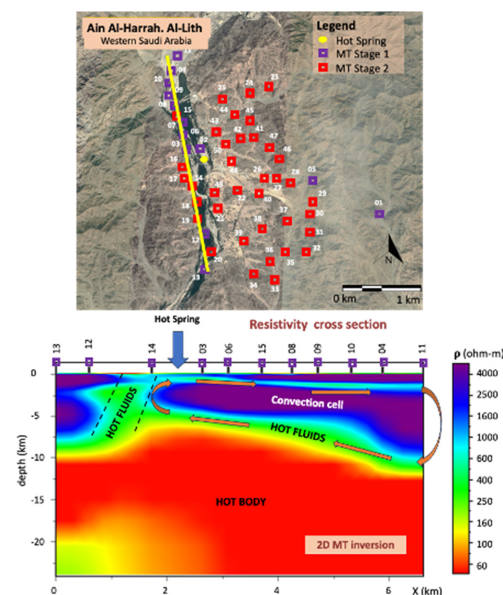


Figure 20. Two-dimensional geoelectrical model presenting the geothermal system in Al-Lith area, Saudi Arabia. In the low-resistivity hot body, the hot fluids form the heat exchanger of a convection cell. The fracture zone depicted with dashed lines acts as the pathway for the hot fluids to reach the surface. The arrow shows the hot spring at the top section. Above the section is a map showing the location of MT sites. The purple rectangles along the hot spring (yellow line) represent the sites displayed on the profile.

A fluid cell of lower resistivity and a deeper heat source can be identified from the MT data. The blue arrow in the figure indicates the location of a known hot spring as a reference.

Future activities in this project include other geophysical measurements (gravity, passive seismic, CSEM) with denser station spacings and data integration.

2.3. Enhanced Oil Recovery (EOR)

Imaging a flood front can often increase the EOR recovery factor by 30%–50% [23], which means less carbon footprint per barrel produced. When using CO₂ as a driving gas, one can obtain further carbon credits and move toward CO₂-neutral operations. From an EM plume imaging sensitivity viewpoint, EOR lies between CCUS and geothermal energy, as in most cases an unbiased resistivity of the fluids at the boundary of the flood front is needed. The first example is a heavy oil application where oil reservoirs are often shallow and expensive, and steam is used to drive the oil. This scenario represents a resistivity contrast at the flood front that would be replaced in case of CO₂ flooding with a short conductive front followed by a resistive CO₂ plume. The second key issue in the EOR case is the ability to record EM signals through the casing. This issue can be overcome by using a surface-to-borehole configuration. Another typical EOR case is waterflood, where a strong contrast between the resistive oil and the conductive water is present. We show a field example for this supported by 3D modeling.

Figure 21 shows a typical resistivity section for a heavy-oil (HO) reservoir in the Middle East. In this case, the oil reservoir is shallow, around 250–350 m depth. The oil is routinely driven by expensive steam (conductive oil–water contact—OWC). Using CO₂ would add carbon credit to the equation and produce resistive oil–gas contact (OGC). The critical considerations are to map the HO reservoir versus the free water zone below, which is a conductive target, and to map oil leaks from the HO reservoir into the upper aquifer, which is a resistive target. Thus, all EM components are required. We modeled these scenarios using shallow borehole measurements as they provided a better image of the anomaly [66]. The results are shown at the bottom of Figure 21 with the electric field in line with the transmitter, Ex, the vertical electric field, Ez, just 10 m below the surface, and the time derivative of the magnetic field dBz/dt at the surface. The top curve represents the field values flooded and unflooded (dashed) and below the percentage variation for different times after turn-off. The water flood is clearly seen in all curves—slightly smoother for the magnetic field and most expressed for the vertical electric field. This is because of the focusing effect that shallow boreholes show.

After obtaining large anomalies with shallow boreholes, the next step in the modeling exercise is to assess the EM response when the boreholes are connected to the surface. This is because much larger source moments and signals at the surface can be more easily generated than in the borehole. Furthermore, a better signal-moving receiver in the borehole can be obtained as they are more protected from surface EM noise. Figure 22 depicts the surface-to-borehole concept with a transmitter at the surface (sketch on the bottom right of the figure). In this figure, the same components as in Figure 21 are analyzed, except this time in the frequency domain (casing effects are frequency-dependent), where real and imaginary parts of the solution can be compared, with and without steel casing, and using Finite Difference (FE) and Finite Element (FD) software codes. Here, we compared FD and FE codes. Their responses were in good agreement. The electric and magnetic fields in the borehole give additional insight into the required measurements. To a depth of 2500 m, the signal level from a surface transmitter is well above the noise floor. For magnetic field components, sensors already in production can be used. The magnetic field is in the micro-Tesla range, while typical fluxgate sensors have a 3–6 pico-Tesla noise floor. Therefore, extending the borehole sensors from a shallow borehole tool to a deep one is feasible.

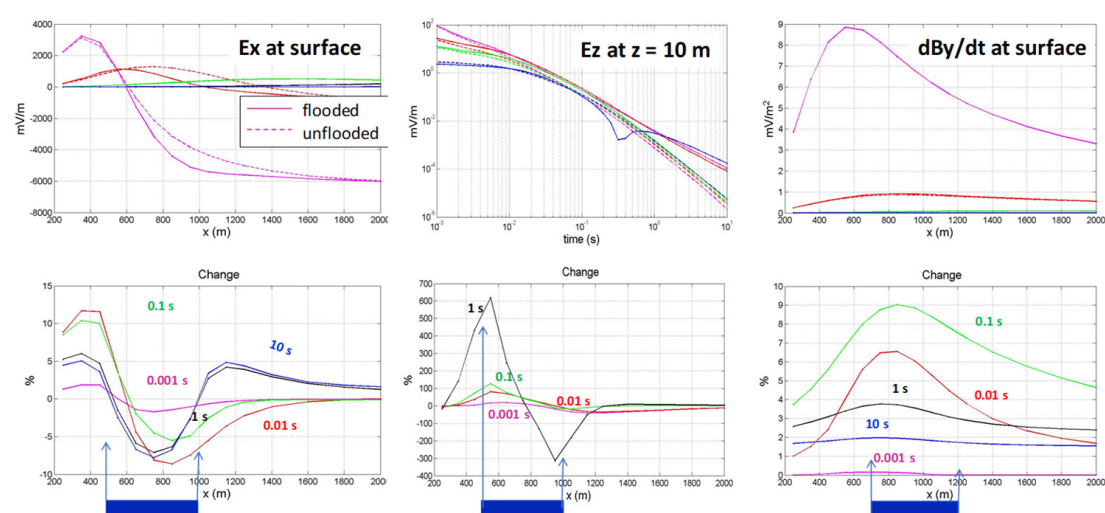
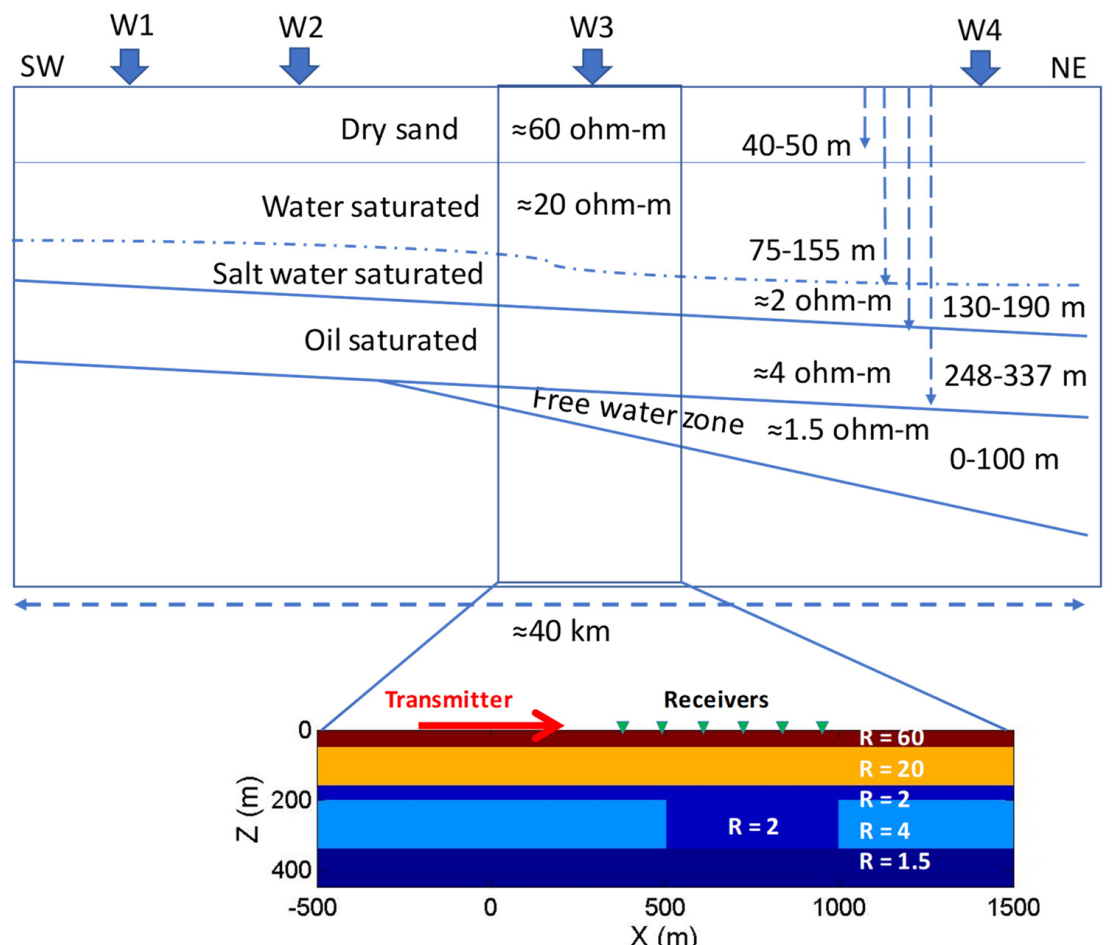


Figure 21. Heavy oil EOR flood model (**top**) and results (**bottom**). The model represents a typical shallow heavy oil model where conductors (water/steam flood) and resistors (heavy oil) must be mapped. Four wells were considered (W1, W2, W3, and W4). The practical components (surface electric and magnetic fields and vertical borehole electric field) are shown below. The oil-saturated and flooded reservoir response curve is displayed below the percentage variation due to flooding (modified after [67]). The thicknesses of the model's layers are shown on the model's right side. The reservoir is represented by the blue rectangles at the bottom of the figures depicting the percentage of variation.

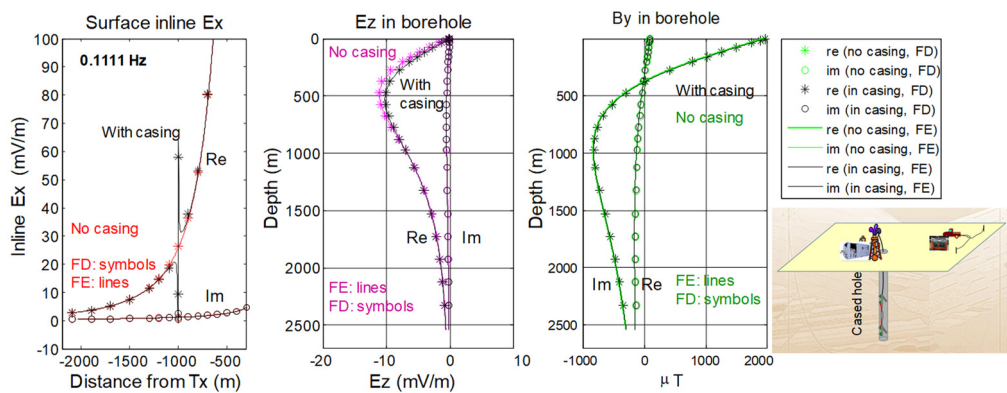


Figure 22. Verification of 3-dimensional modeling results for casing surface-to-borehole applications. The practical field components, surface electric and magnetic fields, and the vertical electric field in the borehole are shown (After [68]).

This example shows that it is possible to obtain meaningful data from the surface, and borehole sensors can contribute with a good EM response using existing technology.

The second example illustrates the surface applications using test measurements from an oil field. Figure 23 shows an exemplary layout across a reservoir (gray outline) with the flood front surface projection shown by the blue line. Ideally, one would deploy as many receivers as possible, but cost/logistics limitations often only allow limited use. Microseismic receivers were included as microseismic data can be easily acquired with the same data acquisition system.

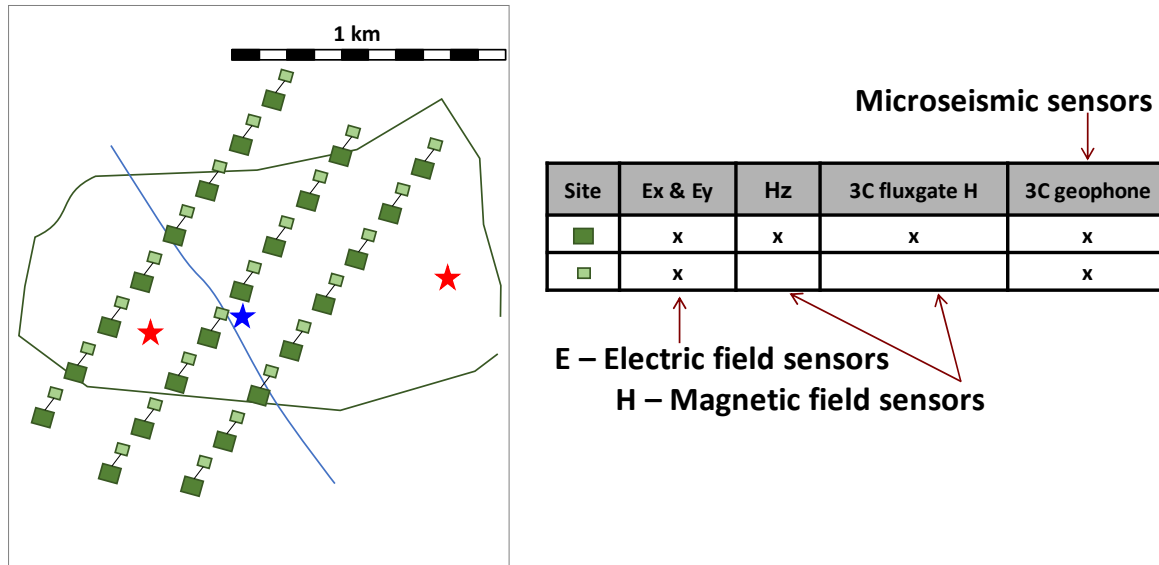


Figure 23. Example of a survey plan for an EOR waterflood using multiple receivers. The blue line represents the waterfront projection to the surface. Blue star: water injection well. Red stars: Production wells. The table shows details of the EM and seismic receivers. The green outline is the surface projection of the oil reservoir.

Figure 24 shows some test data from a water flood field test. The raw data are aligned with the transmitter current, and the seismic traces are moved to the seismic processing. The electric field at the top left of Figure 24 follows the transmitter current. The magnetic field shows the transients resulting from the transmitter and the noise recorded by the receivers. The top right depicts the stacked signal before and after filtering. In the figure's middle and bottom row, the flowcharts for processing and inversion/interpretation, respectively, are

shown. In this survey, the generator noise had to be filtered out during the data processing. The field tests started with careful site selection and feasibility analysis, as described in the CCUS example.

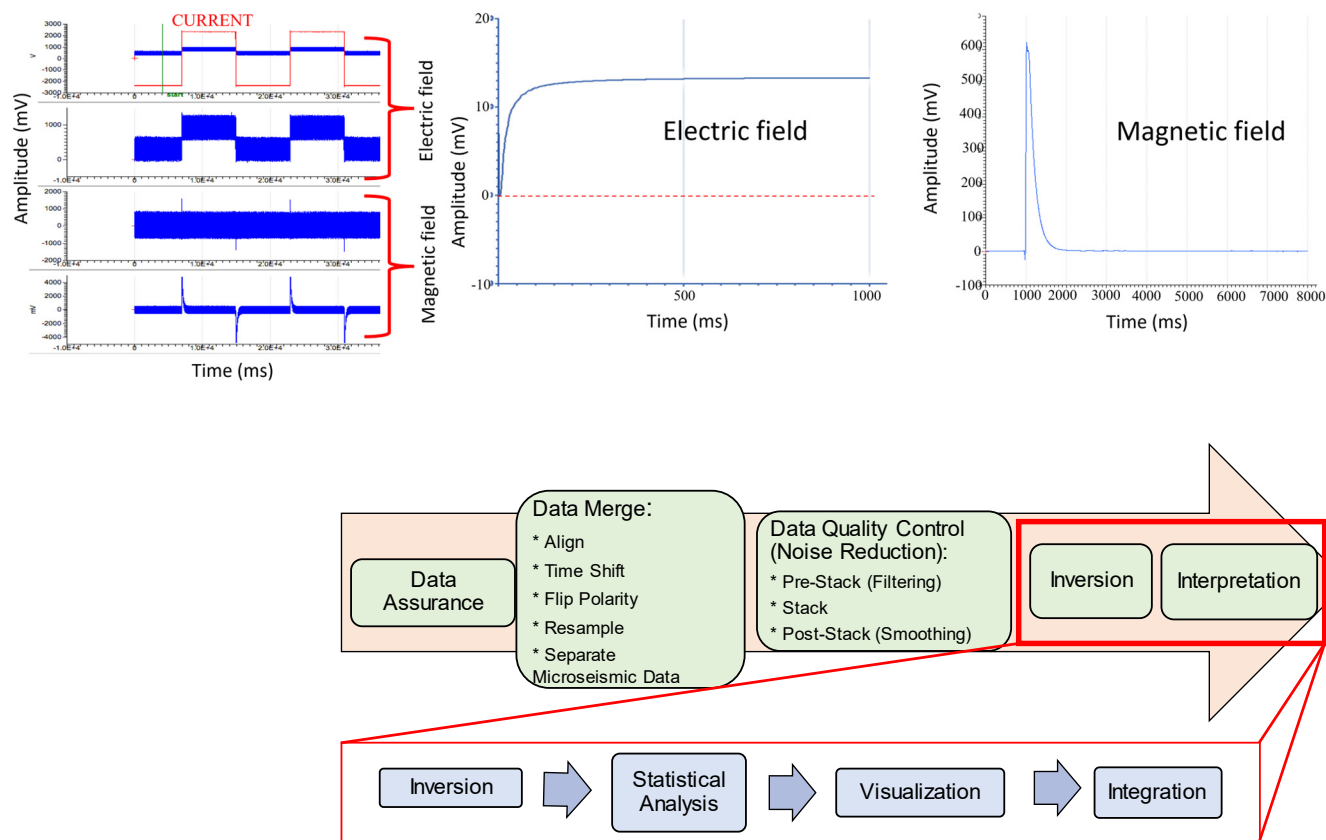


Figure 24. Data processing example from the EOR waterflood field test. The top shows (from left to right) the raw data sequences for receivers and transmitters (CURRENT). Stacked data for the electric and magnetic fields are shown. Below is the processing workflow and inversion/interpretation workflow.

The results from the field trial are shown in Figure 25. The survey layout was a 1 km long transmitter and several receivers crossing the waterflood at a 2.5 km distance. One receiver is directly above the waterflood, which consists of water injection at 2 km depth from horizontal wells. The second receiver is 400 m away from the first one. Displayed are the time derivatives of the magnetic field as a time-lapse difference in percent over approximately 50 h. Whereas the receiver directly above the water flood showed a 30% anomaly, the second only showed 2%, which we attributed to noise (our threshold in this experiment). The same responses from 3D modeling of the survey results at the bottom of the figure only showed about a 3 to 5% anomaly. Three-dimensional models, including the horizontal well casing and infrastructure, could not explain the difference via modeling. One of the two possible explanations is current channeling, where the induced transmitter current is channeled into the water flood as it covers a sizeable subsurface volume. Another possibility is the flood front related to the pore fluid mechanism described in Figure 1. When the flood front replaces fluid, it exerts forces on the old pore fluid, which causes localized alignment of the saturation water and, subsequently, an abrupt resistivity reduction. Further data on this are outstanding.

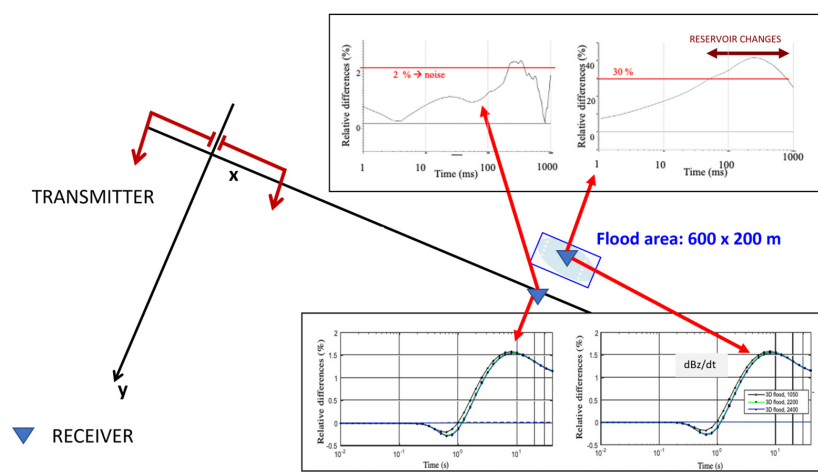


Figure 25. Survey layout and time differences derived from the field data (top curves) and comparative 3D modeling responses (bottom curves).

2.4. Critical Minerals—Lithium Exploration

As discussed above, lithium applications require the same EM technology as in the other case history examples. Mature lithium deposits can be found in Latin America, China, Australia, and the USA, and emerging deposits can be found in Europe and the Middle East [17].

2.4.1. Lithium Exploration in Argentina

In total, 65% of world reserves are in the so-called lithium triangle located in Argentina–Bolivia–Chile. This area hosts salt flats with brines that contain this mineral [69].

Due to the growth of the lithium market, the exploration frontier is changing, and currently, it extends to new concepts that drive toward the exploration of clay deposits with anomalous lithium concentrations, with much shorter production times from brine resources; fractured basements saturated with brine; and deep targets [69,70]. Figure 26 shows a summary of the process leading to lithium deposits. The minerals from mountain ranges combine with water and reach salty flats, where they build salt flats. A field setup of the equipment is shown at the top.

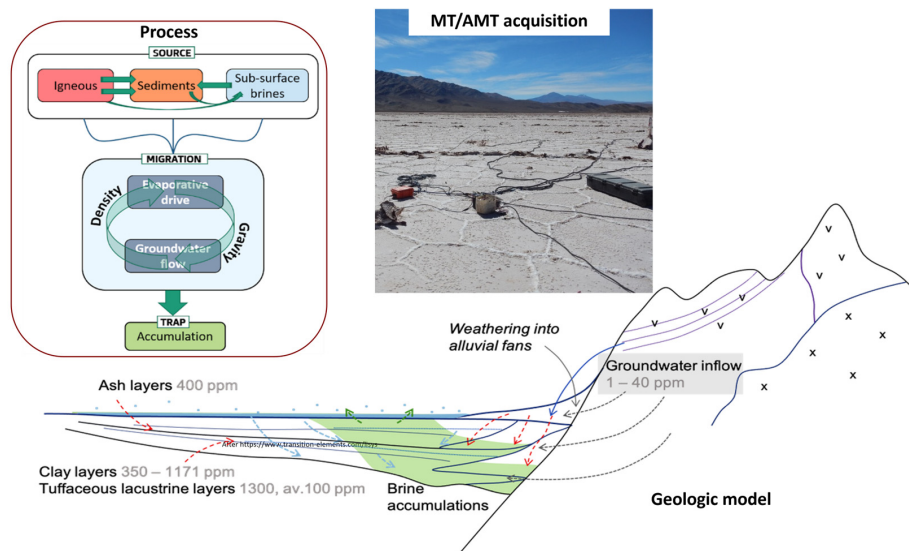


Figure 26. Schematic of lithium generation with the process flow at the top left. At the bottom is a schematic for the generation process where minerals from the mountains are carried to the bottom of the basin, where they meet evaporated salt and build salt flats.

The elements of the lithium-bearing systems require deep imaging of the endorheic (i.e., closed) basins. Geophysical variations, such as low electrical resistivity in salt concentrations, low acoustic impedances, and dynamics of the hydrogeological system, make brine exploration a complex problem. Operationally, the situation is not better because the Argentine salt flats are in sterile areas, at altitudes of 3600–4200 m and more, and, in many cases, in hostile environments with difficult accessibility and surveying. EM methods are better suited for high-conductivity targets, such as lithium brine with low resistivity (typically 0.1 to 0.5 ohm-m), than DC resistivity methods. Due to its limited dynamic range, this resistivity contrast at depth is also challenging for conventional mining and groundwater prospecting equipment.

Curcio et al. [70,71] analyzed different geophysical responses (seismic, magnetics, electric, EM, and gravity) in salt brine exploration. Various feasibility studies, field tests, and previous acquisitions were analyzed, and new acquisitions in many salt flats were made. Full-tensor MT, gravity, and electrical resistivity tomography (ERT) are currently the best combination of geophysical methods to reach the exploration objectives: characterization of the salt flat in-depth, basement delineation, definition of the main structures and main faults with the section, and detection of semi-freshwater aquifers in the edge of the salt flat providing the recharge that is key to the water balance of the endorheic basin.

MT's success in brine exploration relies on the low frequencies at which the MT method operates, compensating for the effect of the low electrical resistivity values in the skin depth relation. Sensitive to conductance, MT prospects the entire conductive column and characterizes the basement. Although the signal may be low, the equipment used in the case history here has patented amplifier behavior [18] and outstanding storage capacity that provides sufficient data statistics, resulting in an enhanced signal-to-noise ratio during advanced data processing [49]. On the other hand, a full-tensor MT provides extra interpretation attributes that cannot be achieved with other EM methods [70,71].

Figure 27 shows the MT response in salt flats. The complete study corresponds to a multi-measurement (full-tensor MT, Gravity, and ERT) survey where the geophysical model was obtained by integrating geophysical data with well data to build a 3D static model and a 3D dynamic model used in the resources and reserves estimation.

The MT frequency bandwidth is from 0.001 to 50 Hz. In both interpretations, the polar diagrams and skew indicate a 2D/3D dimensionality, and the MT section is divided into three geophysical units: the highest electrical resistivity (in red) is interpreted as the basement; the electrical resistivity in blue-violet (with the lowest resistivity of 0.1 ohm-m to 1 ohm-m) is interpreted as brine-saturated rock or wet clay (only possible—in principle); and green (mid resistivity) interpreted as rock saturated with fresh water with a lower content of salinity than the violet unit.

The first example is in the Arizaro salt flat. During 2019, approximately 65 km of full-tensor MT data with a depth of investigation of 2 km were acquired. Figure 27 (top) shows the 2D section of one of the ten lines. The MT section shows that the signal successfully passed the conductive unit that in the west has 200 m thickness, whereas the center-east model reaches 400 m depth. The model shown also delineates the shallower basement in the east (3000 m depth) and deeper in the west (2400 m depth) and main faults.

In the second example, approximately 50 km of full-tensor MT data with a depth of investigation of 2 km were acquired in the Pozuelos salt flat (bottom in Figure 27) in 2019. Figure 27 (bottom) shows the 2D section of one out of seven lines. Two conductive units, the shallower one from the surface, can reach 400 m thickness except in the NE of the area, where a fault indicates the end of the unit. According to the production wells, this unit couples a clastic or evaporite multilayer system where most of them are saturated with brine. The shallower portion of the mid-zone of the model has mid-resistivity values that indicate a zone of recharging with low-salinity water. The deeper conductive unit can reach a thickness of 500 m in the middle-NE part of the model. This unit and an important reverse fault are also detected in the crosslines. Still, we cannot affirm if its low conductivity

is due to a deeper multilayer system saturated with brine or if it is due to wet clay (unlikely) because the wells are shallower than 500 m.

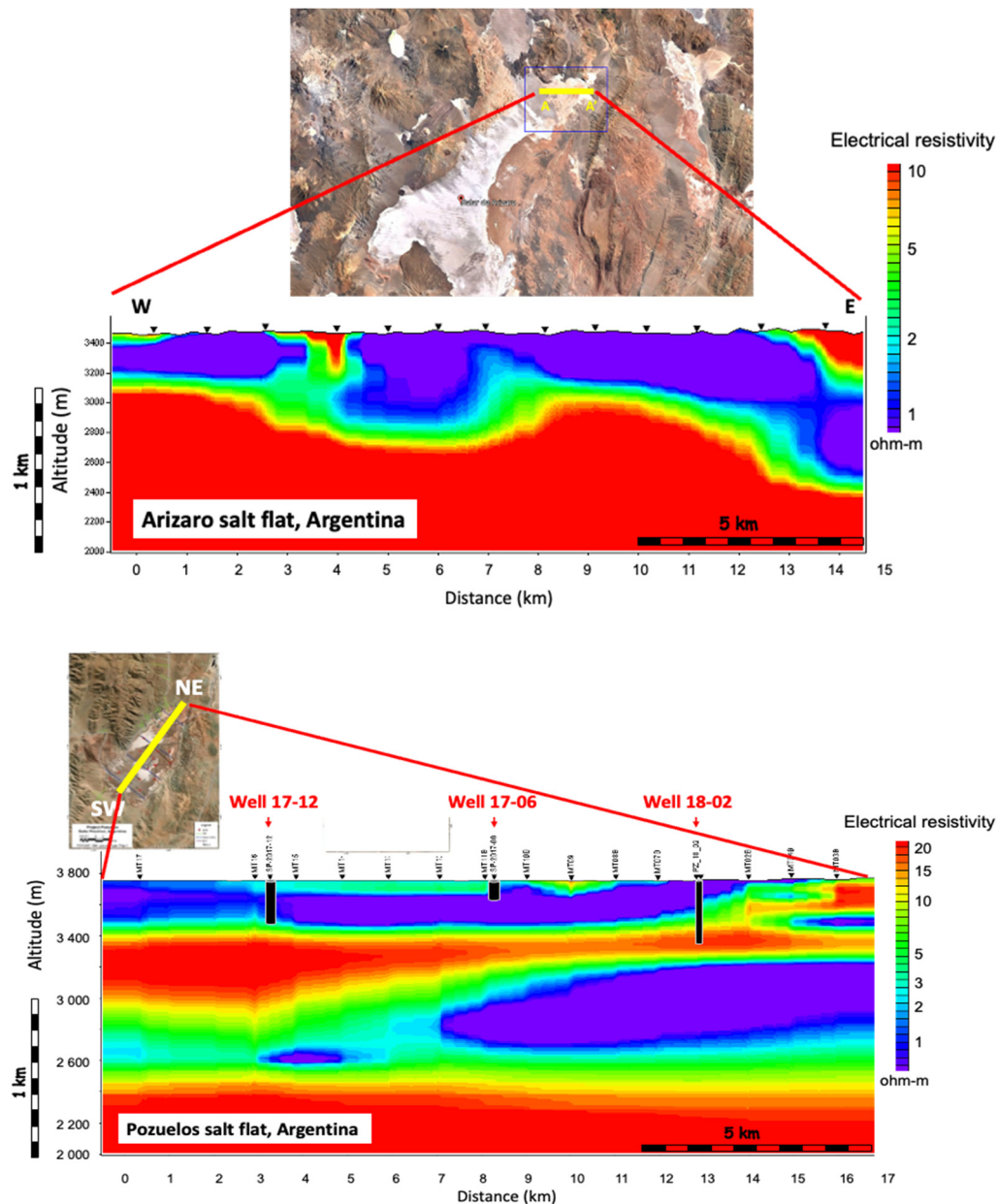


Figure 27. Two 2D resistivity cross sections, including the location of the two surveys are displayed.

2.4.2. Lithium Exploration in Saudi Arabia

Active and passive electromagnetic surveys (CSEM-LOTEM and MT) were conducted in the Half-Moon region of East Province in Saudi Arabia in January 2022 [17]. A high-power CSEM transmitter using a 1 km dipole was installed for the energy transmission, and seven receivers for both active and passive EM measurements were deployed at various distances from the transmitter, ranging from 930 m to 20 km. A 250 kVA generator was connected to the transmitter's switch box to inject current through the electrodes. The injected current varied between 40 and 200 Amperes. In addition, the duration of the injection current varied between 5 and 30 min. Four electric field electrodes (Ex_1 , Ex_2 , Ey_1 , Ey_2) and three magnetic coils (H_x , H_y , H_z) were utilized for MT.

For the CSEM survey, two different acquisition geometries and protocols were used. The LOTEM standard CSEM layout with air loop, S20 coil, which measures the vertical time

derivative of the magnetic field, and for the focused-source EM (FSEM), four electric fields with air loop. The objective of the FSEM method is to obtain deep vertical resistivity data with horizontal electric differential field measurements. FSEM enhances the conventional CSEM technique, which has significantly higher spatial resolution and provides resistivity data with greater depth [66,72]. The CSEM (active) measurements were recorded with a 1 kHz sampling frequency during the day and switched to MT (passive) measurements with a 40 Hz sampling rate at night. However, we also utilized MT data sampled at 1 kHz before and after the transmitter was turned on. Both measuring modes (MT and CSEM) displayed a clear signal for all E-field and H-field components installed.

During data acquisition, the recorded signal is the combination of the induced field for the passive source and injected transmitter current for CSEM with the effect of the signal generation process and the Earth's response [22,73–75]. Since two distinct EM measurements were collected, CSEM as an active method and MT as a passive method, the data must be separated and independently processed before they can be interpreted to create a unique subsurface model. The data were processed to perform data quality assurance and data quality control, including filtering. Since the records of the receivers contain both EM measurements with different frequency rates, these must be separated by cropping and merging before quality control processing. MT data generated the impedance, tipper, and spectral density matrices in EDI files conforming to the SEG standard. A one-dimensional (1D) analysis was performed on MT and CSEM (LOTEM) data for each sounding. The 1D inversion for MT data was performed for XY, YX, and the invariant of both data using Occam's inversion technique. The 1D inversion results for MT data with RMS values between 1.3 and 5.3 for a 3-to-5-layer model were estimated. The 1D inversion for the LOTEM-CSEM data was also performed. Both electric and magnetic field data were inverted. Ultimately, both LOTEM and MT data inversion results were compared. The final inverted models indicate that the predicted model from LOTEM and the MT results agreed, as shown in Figure 28. The fit of the CSEM data to the inversion models was generally satisfactory, falling within 1.5% root-mean-square deviation (RMS).

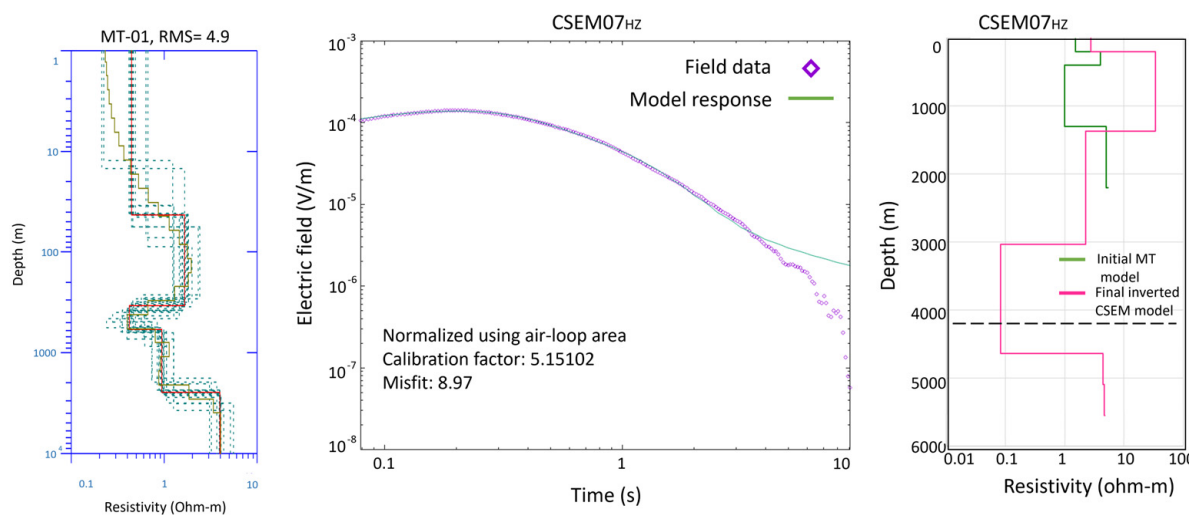


Figure 28. MT and CSEM data inversion results. Left: 1D inversion result at MT-01 location, 1 km away from the transmitter; center: the fitting between the modeled and observed E-field in CSEM-07, 20 km away from the Tx, is presented; right: the final inverted model is shown for CSEM-07 location using MT-01 location results as an initial model for the inversion. The skin depth at 4.1 km is shown as a dashed line (after [68]).

All MT data closest to the transmitter (Tx) were inverted using a five-layer model as a starting model, and the final inverted model exhibited similar behavior. In all four soundings below 300–350 m, a layer with a resistivity of less than one ohm-m was detected. The bedrock, identified as the more resistive formation, is two kilometers below the surface.

The final inverted resistivity from the MT data at the same station was used as the initial model for the CSEM inversion. At a depth of 300–350 m below the surface of the Earth, a resistivity of approximately 0.3 ohm-m was observed, and a thickness of nearly 1 km was detected.

Similarly, the processed MT data collected 20 km from the transmitter (Tx) were used as the initial model for the final 1D inversion of the collected CSEM data in ST-07. Final inverted models for ST-07 are nearly identical, indicating that the data quality, 20 km away from Tx, was surprisingly high. At a depth of 1.65 km beneath the Earth's surface, a layer with a resistivity of approximately 0.6 ohm-m and a thickness of nearly 1.9 km was detected.

The study area's high-resolution MT/CSEM survey detected a very low resistivity anomaly with values around 0.3 ohm-m, similar to seawater resistivity. As no water layer is at depth, resistivities as low as 0.3 ohm-m can be linked to lithium deposits.

Both lithium applications showed unusually low resistivity. Future drilling will confirm the measurements.

3. Discussion

The concept of using CSEM for fluid imaging is based on a carefully designed workflow supported by a sensitive acquisition system. A critical aspect of the workflow is the flexibility to select numerous calibration points. The models and data are checked against a 3D anisotropic model derived from the logs at these points. This model—verified by 3D modeling—represents the ground truth. The feasibility analysis includes on-site noise measurements to determine the optimum survey parameters and acquisition time to obtain the best signal-to-noise ratios in the data.

We selected four energy transition applications (CO_2 monitoring, geothermal, EOR, and lithium exploration) where this concept and the system architecture led to successfully reaching the objectives. At the CO_2 monitoring site in North Dakota, we thoroughly applied the workflow and, under the inclusion of all logs, derived full 3D anisotropic modeling consistent with lithology, seismic data, and all other logs. The model serves as the ground truth for verifying data acquisition, quality assurance (near-real data quality check and acquisition operations control), and inversion.

For the geothermal example in Saudi Arabia, we used integrated geology and multi-measurement (EM [MT & CSEM], gravity, and passive seismic) information to overcome the lack of deep boreholes. The initial results already explain the known geothermal system around a hot spring area, and further data and interpretation are to follow.

Applying this workflow to EOR, where numerous boreholes exist in an oil field environment, brings challenges associated with the oil field noise and operation restrictions. The feasibility allowed us to design the field test so that we could overcome these difficulties and see the injection flood front after only a few days of recording.

The same EM system was applied to lithium exploration in Argentina (MT) and Saudi Arabia (MT and CSEM). In Argentina, the system could map existing lithium deposits. In Saudi Arabia, the MT and CSEM recorded at several locations showed unusually low resistivity conductors, strongly indicating that lithium deposits are possible.

In this CCUS application, both electric and magnetic fields gave comparable information. The magnetic field was more susceptible to noise. The information content down to a depth of 3 km was verified by analyzing the eigenvalues in the inversion. Due to the extensive calibration effect of the measurements, hardware, and methodology, the data were interpreted fully automatically, with the results matching the 3D model adjusted for the seismic horizons matching all CSEM components.

The EM application to EOR is more complex than for CCUS. In most cases, both electric and magnetic components are required. Also, the signal bandwidth is larger as the depth of hydrocarbon reservoirs can vary from a few hundred to a few kilometers. Resolution can be increased by adding borehole measurements. This is important as we get closer to the ground truth of a reservoir and decision making.

4. Conclusions

The successful use of CSEM for fluid imaging for CCUS, EOR, geothermal, and lithium applications illustrates its value. The data acquisition system consisting of MT and CSEM components was based on the careful design of high-fidelity hardware coupled with a monitoring architecture that delivers repeatable measurements within an overall system repeatability of better than 0.5%. Verification of the results was conducted via integration with borehole logs. The acquisition workflow was tailored to the system so that well logs can be used to verify acquisition results in a near-real-time quality assurance mode. The system consists of MT and CSEM components, and both methodologies are complementary.

The case histories start with a CO₂ monitoring example (baseline measurements), followed by EOR applications with the same principle and workflow. While the data in the EOR example were noisier, the time-lapse anomaly clearly showed the flood front. For geothermal applications, we showed the dynamic geothermal flow cell being already mapped by the MT measurements that were used to design a detailed CSEM follow-up survey. Finally, the changes made to the hardware lead to a high acquisition dynamic that can map lithium brine.

The results of all examples are very significant:

- CCUS plume monitoring: We showed that we could certify the data and data quality within the context of the 3D anisotropic log from the beginning. This process requires extreme care during acquisition and quality assurance. As a result, potential risks can be mitigated, and cost savings can be achieved for the time-lapse measurements. By ensuring the accuracy and quality of data, researchers, practitioners, and decision-makers can make informed decisions based on sound data and analysis.
- Geothermal: The initial MT data have demonstrated a coherent match with all geological models derived for the hot spot area, attesting to the accuracy and reliability of the data obtained. This suggests that additional measurements, including CSEM measurements, will facilitate future drilling. The high data quality gives us a strong sense of optimism about the future success of the EM geothermal application.
- EOR case: We worked in existing oil fields and logs, and the noise test yielded a field test design, subsequently confirming that we could see the water flood front and confirmed the anomaly with 3D models.
- The lithium exploration examples from Argentina and Saudi Arabia have revealed a highly conductive layer positioned slightly above 1 km in depth. The data consistency indicates that this layer is probably a lithium brine (a typical finding in Argentina). We expect these results will stimulate more interest in the possibility of lithium exploration in Saudi Arabia.

Author Contributions: Conceptualization and lead writing, C.B.-O., A.C., P.S. and K.S.; methodology, K.S., Y.M. and A.Y.P.; 3D modeling, S.D.; Case histories—A.C., C.B.-O., D.C.A., R.J.K., K.S., P.S. and W.D.P. All authors have read and agreed to the published version of the manuscript.

Funding: The North Dakota case study research was funded by the U.S. Department of Energy (DOE) National Energy Technology Laboratory (NETL) as part of Cooperative Agreement DE-FE0031889 and supported by Minnkota Power Cooperative and the Energy & Environmental Research Center (EERC) of the University of North Dakota. King Fahd University of Petroleum and Minerals (KFUPM) funded the work in Saudi Arabia. Litica Resources SA supported the work in Argentina. KMS Technologies funded field tests, equipment, and interpretation development.

Data Availability Statement: The data are not available. The DOE-funded data will be made available in due course.

Acknowledgments: The authors thank the U.S. Department of Energy National Energy Technology Laboratory for funding the North Dakota case study research. The authors also thank Minnkota Power Cooperative for supporting the North Dakota case study and our colleagues at EERC, KMS Technologies, and KFUPM for contributing to this paper. PROINGEO SA performed the work in Argentina.

Conflicts of Interest: The authors declare no conflict of interest.

Appendix A

Some complementary information related to field data acquisition and data processing, interpretation, and inversion activities in the case histories is presented in this appendix: Cloud-connected quality assurance is described in detail in [76]. MT data were processed using methods described in [49] and the CSEM processing described in [50]. The 1D, 2D, and 3D inversion using inversion statistics are described by [28,77–80]. MT and CSEM inversion was conducted using an algorithm from [80]. The 3D anisotropic CSEM modeling is based on ([25,81] for reference summary). The MT inversion module is based on [77–80].

References

- IEA. Energy Technology Perspectives 2023, IEA, Paris. 2023. Available online: <https://www.iea.org/reports/energy-technology-perspectives-2023> (accessed on 1 February 2023).
- IEA. Energy Technology Perspectives 2020, IEA, Paris. 2020. Available online: <https://www.iea.org/reports/energy-technology-perspectives-2020> (accessed on 1 February 2023).
- Azzolina, N.A.; Nakles, D.V.; Gorecki, C.D.; Peck, W.D.; Ayash, S.C.; Melzer, L.S.; Chatterjee, S. CO₂ storage associated with CO₂ enhanced oil recovery: A statistical analysis of historical operations. *Int. J. Greenh. Gas Control* **2015**, *37*, 384–397. [\[CrossRef\]](#)
- Benson, S.M.; Cole, D.R. CO₂ Sequestration in Deep Sedimentary Formations. *Elements* **2008**, *4*, 325–331. [\[CrossRef\]](#)
- Available online: <https://www.netl.doe.gov/carbon-management/carbon-storage/faqs/carbon-storage-faqs> (accessed on 15 January 2023).
- Barbier, E. Geothermal energy technology and current status: An overview. *Renew. Sustain. Energy Rev.* **2002**, *6*, 3–65. [\[CrossRef\]](#)
- Babaei, M. Integrated Carbon Sequestration–Geothermal Heat Recovery: Performance Comparison Between Open and Close Systems. *Transp. Porous Med.* **2019**, *126*, 249–273. [\[CrossRef\]](#)
- Randolph, J.B.; Saar, M.O. Combining geothermal energy capture with geologic carbon dioxide sequestration. *Geophys. Res. Lett.* **2011**, *38*, L10401. [\[CrossRef\]](#)
- Randolph, J.B.; Saar, M.O. Coupling carbon dioxide sequestration with geothermal energy capture in naturally permeable, porous geologic formations: Implications for CO₂ sequestration. *Energy Procedia* **2011**, *4*, 2206–2213. [\[CrossRef\]](#)
- Buscheck, T.A.; Elliot, T.R.; Celia, M.A.; Chen, M.; Sun, Y.; Hao, Y.; Lu, C.; Aines, R.D. Integrated Geothermal-CO₂ Reservoir Systems: Reducing Carbon Intensity through Sustainable Energy Production and Secure CO₂ Storage. *Energy Procedia* **2013**, *37*, 6587–6594. [\[CrossRef\]](#)
- Weiss, C.J.; Jones, A.G. Introduction to this special section: Critical minerals exploration. *Lead. Edge* **2023**, *42*, 236. [\[CrossRef\]](#)
- Barajas-Olalde, C.; Mur, A.; Adams, D.C.; Jin, L.; He, J.; Hamling, J.A.; Gorecki, C.D. Joint impedance and facies inversion of time-lapse seismic data for improving monitoring of CO₂ incidentally stored from CO₂ EOR. *Int. J. Greenh. Gas Control* **2021**, *112*, 103501. [\[CrossRef\]](#)
- Boerner, J.H.; Herdegen, V.; Repke, J.-U.; Spitzer, K. The electrical conductivity of CO₂-bearing pore waters at elevated pressure and temperature: A laboratory study and its implications in CO₂ storage monitoring and leakage detection. *Geophys. J. Int.* **2015**, *203*, 1072–1084. [\[CrossRef\]](#)
- Carlson, M.R. An Analysis of the Caprock Failure at Joslyn. In Proceedings of the SPE Heavy Oil Conference in Calgary, Calgary, AB, Canada, 12–14 June 2012. [\[CrossRef\]](#)
- Strack, K.; Davydychova, S.; Hanstein, T.; Paembonan, A.Y.; Smirnov, M. An array multiphysics acquisition system with focus on reservoir monitoring for the energy transition. *Earth Environ. Sci. Res. Rev.* **2022**, *5*, 237–268. [\[CrossRef\]](#)
- Sheriff, R.E. *Encyclopedic Dictionary of Applied Geophysics*; Society of Exploration Geophysicists: Houston, TX, USA, 2002; p. 429.
- Ashadi, A.L.; Martinez, Y.; Kirmizakis, P.; Hanstein, T.; Xu, X.; Khogali, A.; Paembonan, A.Y.; AlShaibani, A.; Al-Karnos, A.; Smirnov, M.; et al. First High-Power CSEM Field Test in Saudi Arabia. *Minerals* **2022**, *12*, 1236. [\[CrossRef\]](#)
- Jiang, J.; Aziz, A.A.; Liu, Y.; Strack, K.M. Geophysical Acquisition System. U.S. Patent 9,057,801, 2015.
- Peck, W.D.; Ayash, S.C.; Klapperich, R.J.; Gorecki, C.D. The North Dakota integrated carbon storage complex feasibility study. *Int. J. Greenh. Gas Control* **2019**, *84*, 47–53. [\[CrossRef\]](#)
- Sarnoski, A.H. The Stratigraphy and Depositional History of the Deadwood Formation, with a Focus on Early Paleozoic Subsidence in the Williston Basin. Master’s Thesis, Grand Forks, University of North Dakota, Grand Forks, ND, USA, 2015.
- Le Fever, R.D. Sedimentology and Stratigraphy of the Deadwood-Winnipeg Interval (Cambro-Ordovician), Williston Basin. Paleozoic Systems of the Rocky Mountain Region; Golden, The Rocky Mountain Section (SEPM), 1996; Available online: https://archives.datapages.com/data/rocky_sepm/data/034/034001/11_rocky_mount340011.htm?q=%2BtextStrip%3Adeposition+textStrip%3Aenvironment+textStrip%3Astratigraphy+textStrip%3Anorth+textStrip%3Awestern+textStrip%3Adesert+textStrip%3Aegypt+-isMeetingAbstract%3Amtgabsyes (accessed on 1 September 2023).
- Strack, K. *Exploration with Deep Transient Electromagnetics*; Elsevier: Amsterdam, The Netherlands, 1992; ISBN 978-0444895417.
- Strack, K.-M. Future directions of Electromagnetic Methods for Hydrocarbon Applications. *Surv. Geophys.* **2014**, *35*, 157–177. [\[CrossRef\]](#)

24. Barajas-Olalde, C.; Davydycheva, S.; Hanstein, T.; Laudal, D.; Martinez, Y.; MacLennan, K.; Mikula, S.; Adams, D.C.; Klapperich, R.J.; Peck, W.D.; et al. Using controlled-source electromagnetics (CSEM) for CO₂ storage monitoring in North Dakota CarbonSAFE project. In *First International Meeting for Applied Geoscience & Energy Expanded Abstracts*; Society of Exploration Geophysicists: Tulsa, Oklahoma, 2021; pp. 503–506. [CrossRef]
25. Davydycheva, S.; Druskin, V. *Staggered Grid for Maxwell's Equations in Arbitrary 3-D Inhomogeneous Anisotropic Media*; Oristaglio, M., Spies, B., Eds.; Three-Dimensional Electromagnetics—Society of Exploration Geophysicists: Tulsa, Oklahoma, 1999; pp. 119–137.
26. He, Z.; Liu, X.; Qiu, W.; Zhou, H. Mapping reservoir boundary by borehole-surface TFEM: Two case studies. *Lead. Edge* **2006**, *24*, 896–900. [CrossRef]
27. Tietze, K.; Ritter, O.; Veeken, P. Controlled-source electromagnetic monitoring for reservoir oil saturation using a novel borehole-to-surface configuration. *Geophys. Prospect.* **2015**, *63*, 1–23. [CrossRef]
28. Thiel, S. Electromagnetic monitoring of hydraulic fracking relationship to permeability, seismicity, and stress. *Surv. Geophys.* **2017**, *38*, 1133–1169. [CrossRef]
29. Kalscheuer, T.; Juhojuntti, N.; Vaittinen, K. Two-Dimensional Magnetotelluric Modeling of Ore Deposits: Improvements in Model Constraints by Inclusion of Borehole measurements. *Surv. Geophys.* **2018**, *39*, 467–507. [CrossRef]
30. Keller, G.V.; Frischknecht, F.C. *Electrical Methods in Geophysical Prospecting*; Pergamon Press: Oxford, UK, 1967.
31. Strack, K.; Barajas-Olalde, C.; Davydycheva, S.; Martinez, Y.; Paembanan, A.Y. CCUS plume monitoring: Verifying surface CSEM measurements to log scale. In Proceedings of the SPWLA 64th Annual Logging Symposium, Conroe, TX, USA, 10–14 June 2023.
32. Doveton, J.H. *Log Analysis of Subsurface Geology Concepts and Computer Methods*; Kansas Geological Survey: Lawrence, Kansas, 1986.
33. Han, D.; Batzle, M. Velocity, Density, and Modulus of Hydrocarbon Fluids—Empirical Modeling. In *SEG Technical Program Expanded Abstracts*; SEG: Houston, TX, USA, 2000; pp. 1867–1870.
34. National Institute of Standards and Technology. 2021. Available online: <https://webbook.nist.gov/chemistry/fluid/> (accessed on 15 March 2023).
35. Yan, W.; Huang, S.; Stenby, E.H. Measurement and modeling of CO₂ solubility in NaCl brine and CO₂-saturated NaCl brine density. *Int. J. Greenh. Gas Control* **2011**, *5*, 1460–1477. [CrossRef]
36. Han, D.; Sun, M. Velocity and Density of Water with Dissolved CH₄ and CO₂. In *SEG Technical Program Expanded Abstracts*; SEG: Houston, TX, USA, 2013; pp. 2846–2850.
37. Lebedev, M.; Bilenko, O.; Mikhaltsevitch, V.; Pervukhina, M.; Gurevich, B. Laboratory measurements of ultrasonic velocities in CO₂ saturated brines. *Energy Procedia* **2014**, *63*, 4273–4280. [CrossRef]
38. Knight, R.; Dvorkin, J.; Nur, A. Acoustic signatures of partial saturation. *Geophysics* **1998**, *63*, 132–138. [CrossRef]
39. Alemu, B.L.; Aker, E.; Soldal, M.; Johnsen, Ø.; Aagaard, P. Influence of CO₂ on rock physics properties in a typical reservoir rock—A CO₂ flooding experiment of brine saturated sandstone in a CT-scanner. *Energy Procedia* **2011**, *4*, 4379–4386. [CrossRef]
40. Adams, D.C.; Barajas-Olalde, C.; Peck, W.D.; Klapperich, R.J.; Hamling, J.A. On the quantitative CO₂ subsurface monitoring: Rock physics for CO₂ storage and CO₂ EOR. In Proceedings of the 16th Greenhouse Gas Control Technologies Conference (GHGT-16), Lyon, France, 23–24 October 2022; Available online: <https://ssrn.com/abstract=4276978> (accessed on 26 October 2022).
41. Barajas-Olalde, C.; Adams, D.C.; MacLennan, K.; Peck, W.D.; Klapperich, R.J.; Hamling, J.A.; Mikula, S.; Martínez, Y.; Strack, K. Toward CO₂ Multi-measurement Geophysical Monitoring in the North Dakota CarbonSAFE Project. In Proceedings of the 16th Greenhouse Gas Control Technologies Conference (GHGT-16), 23–24 October 2022. Available online: <https://ssrn.com/abstract=4276834> (accessed on 26 October 2022).
42. Archie, G.E. The electrical resistivity log as an aid in determining some reservoir characteristics. *Trans. AIME* **1942**, *146*, 54–62. [CrossRef]
43. Glover, P.W.J. Geophysical properties of the near surface Earth—Electrical properties. In *Treatise on Geophysics*, 2nd ed.; Elsevier: Amsterdam, The Netherlands, 2015; Volume 11.
44. Schlumberger. *Log Interpretation Charts*; Schlumberger Wireline & Testing: Midland, TX, USA, 1997.
45. Branch, J.A.; Bartlett, P.N. Electrochemistry in supercritical fluids. *R. Soc. Philos. Trans. A* **2015**, *373*, 2057. [CrossRef] [PubMed]
46. Ceia, M.A.; Carrasquilla, A.A.; Sato, H.K.; Lima, O. Long offset transient electromagnetic (LOTEM) for monitoring fluid injection in petroleum reservoirs—Preliminary results of Fazenda Alvorada Field (Brazil). In Proceedings of the 10th International Congress of the Brazilian Geophysical Society & EXPOGEF 2007, Rio de Janeiro, Brazil, 19–23 November 2007.
47. Strack, K.M.; Aziz, A.A. Advances in electromagnetics for reservoir monitoring. *Geohorizons* **2013**, *18*, 32–44, (special shale issue).
48. Kumar, D.; Hoversten, G.M. Geophysical model response in a shale gas, *Geohorizons. J. Soc. Pet. Geophys. India* **2012**, *16*, 31–37.
49. Smirnov, M.Y. Magnetotelluric data processing with a robust statistical procedure having a high breakdown point. *Geophys. J. Int.* **2003**, *152*, 1–7. [CrossRef]
50. Strack, K.M.; Hanstein, T.; Eilenz, H. TEM data processing for areas with high cultural noise levels. *Phys. Earth Planet. Inter.* **1989**, *53*, 261–269. [CrossRef]
51. Paembanan, A.Y.; Arjwech, R.; Davydycheva, S.; Smirnov, M.; Strack, K.M. An application of TEM around salt dome near Houston, Texas. In Proceedings of the AIP Conference Proceedings, Geneva, Switzerland, 15–20 September 2017; Volume 1861, p. 30006. [CrossRef]
52. Available online: <https://www.irena.org/> (accessed on 1 September 2023).
53. REN21. Renewables 2022 Global Status Report; REN21 Secretariat: 2022; pp. 1–75. Available online: https://www.ren21.net/wp-content/uploads/2019/05/GSR2022_Full_Report.pdf (accessed on 1 September 2023).

54. Ali, A.; Al-Sulaiman, F.A.; Al-Duais, I.N.A.; Irshad, K.; Malik, M.Z.; Shafiullah, M.; Zahir, M.H.; Ali, H.M.; Malik, S.A. Renewable Portfolio Standard Development Assessment in the Kingdom of Saudi Arabia from the Perspective of Policy Networks Theory. *Processes* **2021**, *9*, 1123. [[CrossRef](#)]
55. Al-Dayel, M. Geothermal Resources in Saudi Arabia. *Geothermics* **1988**, *17*, 465–476. [[CrossRef](#)]
56. Lashin, A.; Chandrasekharam, D.; Al Arifi, N.; Al Bassam, A.; Varun, C. Geothermal Energy Resources of Wadi Al-Lith, Saudi Arabia. *J. Afr. Earth Sci.* **2014**, *97*, 357–367. [[CrossRef](#)]
57. Chandrasekharam, D.; Lashin, A.; Al Arifi, N.; Al Bassam, A.A.; Varun, C. Evolution of Geothermal Systems around the Red Sea. *Environ. Earth Sci.* **2015**, *73*, 4215–4236. [[CrossRef](#)]
58. Chandrasekharam, D.; Lashin, A.; Al Arifi, N. The Potential Contribution of Geothermal Energy to Electricity Supply in Saudi Arabia. *Int. J. Sustain. Energy* **2016**, *35*, 824–833. [[CrossRef](#)]
59. Demirbas, A.; Alidrisi, H.; Ahmad, W.; Sheikh, M.H. Potential of Geothermal Energy in the Kingdom of Saudi Arabia. *Energy Sources Part A Recovery Util. Environ. Eff.* **2016**, *38*, 2238–2243. [[CrossRef](#)]
60. Aboud, E.; Arafa-Hamed, T.; Alqahtani, F.; Marzouk, H.; Elbarbary, S.; Abdulfaraj, M.; Elmasry, N. The Geothermal Magmatic System at the Northern Rahat Volcanic Field, Saudi Arabia, Revealed from 3D Magnetotelluric Inversion. *J. Volcanol. Geotherm. Res.* **2023**, *437*, 107794. [[CrossRef](#)]
61. Al-Douri, Y.; Waheed, S.A.; Johan, M.R. Exploiting of Geothermal Energy Reserve and Potential in Saudi Arabia: A Case Study at Ain Al Harrah. *Energy Rep.* **2019**, *5*, 632–638. [[CrossRef](#)]
62. Al-Amri, A.M.; Abdelrahman, K.; Mellors, R.; Harris, D. Geothermal Potential of Harrat Rahat, Northern Arabian Shield: Geological Constraints. *Arab. J. Geosci.* **2020**, *13*, 268. [[CrossRef](#)]
63. Lashin, A.; Al Arifi, N. Geothermal Energy Potential of Southwestern of Saudi Arabia “Exploration and Possible Power Generation”: A Case Study at Al Khouba Area–Jizan. *Renew. Sustain. Energy Rev.* **2014**, *30*, 771–789. [[CrossRef](#)]
64. Monged, M.H.E.; Hussein, M.T.; Khater, A.E.M. Elemental and Radiological Aspects of Geothermal Springs and Nearby Soil and Sediment of Al-Lith Area: Concentration and Risk Assessment. *Environ. Earth Sci.* **2018**, *77*, 427. [[CrossRef](#)]
65. Ashadi, A.L.; Tezkan, B.; Yogeshwar, P.; Hanstein, T.; Kirmizakis, P.; Khogali, A.; Chavanidis, K.; Soupios, P. Magnetotelluric Case Study from Ain Al-Harrah Hot Spring, Al-Lith, Saudi Arabia. *Arab. J. Sci. Eng. Rev.* **2023**. [[CrossRef](#)]
66. Strack, K.; Davydycheva, S. Using Electromagnetics to Map Lateral Fluid Variations in Carbonates in SE Asia. In *New Approaches in Engineering Research*; Purenovic, J., Ed.; Book Publisher International, 2021; Volume 2, Available online: <https://stm.bookpi.org/NAER-V2/article/view/2119> (accessed on 1 September 2023).
67. Passalacqua, H.; Davydycheva, S.; Strack, K. Feasibility of multi-physics reservoir monitoring for Heavy Oil. In Proceedings of the SPE International Heavy Oil Conference and Exhibition, Kuwait City, Kuwait, 10–12 December 2018; SPE-193690-MS. [[CrossRef](#)]
68. Strack, K.M.; Barajas-Olalde, C.; Davydycheva, S.; Martinez, Y.; Soupios, P. Surface-to-Borehole Electromagnetics Using an Array System: A Case Study for CO₂ Monitoring and the Energy Transition. In Proceedings of the Paper presented at the SPE Annual Technical Conference and Exhibition, Houston, TX, USA, 1 October 2022. [[CrossRef](#)]
69. Curcio, A. Resources and geophysical opportunities in South America, President’s Page. *Lead. Edge* **2022**, *41*, 228–229. [[CrossRef](#)]
70. Curcio, A.; Chanampa, E.; Cabanillas, L.; Piethe, R. An effective multiphysics toolkit for Lithium prospecting: From geophysics to the static reservoir model in Pozuelos salt flat, Argentina. In Proceedings of the Second International Meeting for Applied Geoscience & Energy, Expanded Abstract, Houston, TX, USA, 28 August–1 September 2022; pp. 1979–1983. [[CrossRef](#)]
71. Curcio, A.; Chanampa, E.; Cabanillas, L.; Piethe, R. An effective multiphysics toolkit for Lithium prospecting: From geophysics to the static reservoir model in Pozuelos salt flat, Argentina. *Interpretation* **2023**, *in press*.
72. Davydycheva, S.; Rykhlin, N. Focused-source electromagnetic survey versus standard CSEM: 3D modeling in complex geometries. *Geophysics* **2011**, *76*, F27–F41. [[CrossRef](#)]
73. Strack, K.M.; Martinez, Y.L.; Passalacqua, H.; Xu, X. Cloud-Based Array Electromagnetics Contributing to Zero Carbon Footprint. In Proceedings of the Offshore Technology Conference, Houston, TX, USA, 1–4 May 42022. [[CrossRef](#)]
74. Davydycheva, S.; Rykhlin, N.; Legeido, P. Electrical-prospecting method for hydrocarbon search using the induced polarization effect. *Geophysics* **2006**, *71*, G179–G189. [[CrossRef](#)]
75. Claerbout, J.F. *Fundamentals of Geophysical Data Processing with Applications to Petroleum Prospecting*; Blackwell Science Inc.: Oxford, UK, 1985; ISBN 978-0865423053.
76. Strack, K.; Davydycheva, S.; Passalacqua, H.; Smirnov, M.Y.; Xu, X. Using Cloud-Based Array Electromagnetics on the Path to Zero Carbon Footprint during the Energy Transition. *J. Mar. Sci. Eng.* **2021**, *9*, 906. [[CrossRef](#)]
77. Jupp, D.L.B.; Vozoff, K. Two-dimensional magnetotelluric inversion: *Geophys. J. R. Astr. Soc.* **1977**, *50*, 333–352. [[CrossRef](#)]
78. Chave, A.; Jones, A. *The Magnetotelluric Method: Theory and Practice*; Cambridge University Press: Cambridge, UK, 2012. [[CrossRef](#)]
79. Simpson, F.; Bahr, K. *Practical Magnetotellurics*; Cambridge University Press: Cambridge, UK, 2005.

80. Smirnova, M.; Shlykov, A.; Asghari, S.F.; Tezkan, B.; Saraev, A.; Yogeshwar, P.; Smirnov, M. 3D controlled-source electromagnetic inversion in the radio-frequency band. *Geophysics* **2022**, *88*, E1–E12. [[CrossRef](#)]
81. Available online: <https://kmstechnologies.com/Publications.html> (accessed on 1 September 2023).

Disclaimer/Publisher's Note: The statements, opinions and data contained in all publications are solely those of the individual author(s) and contributor(s) and not of MDPI and/or the editor(s). MDPI and/or the editor(s) disclaim responsibility for any injury to people or property resulting from any ideas, methods, instructions or products referred to in the content.